Observation of a mesoscale eddy dipole on the northern Madagascar Ridge: Consequences for the circulation and hydrography in the vicinity of a seamount

Patrick Vianello, Steven Herbette, Jean-Francois Ternon, Herve Demarcq, Michael J. Roberts

DSR2_2019_147

Observation of a mesoscale eddy dipole on the northern Madagascar Ridge: consequences for the circulation and hydrography in the vicinity of a seamount

Patrick Vianello[a], Steven Herbette[b,*], Jean-François Ternon[c], Hervé Demarcq[c], Michael J. Roberts[a,d]

a. SA-UK Bilateral Chair: Ocean Science and Marine Food Security, Nelson Mandela University, Port Elizabeth, South Africa
b. Laboratoire d'Océanographie Physique et Spatiale (LOPS), IUEM, Univ. Brest - CNRS - IRD - Ifremer, Brest, France
c. MARBEC, IRD, Univ Montpellier, CNRS, Ifremer, Sète, France
d. National Oceanography Centre, Southampton, United Kingdom
** Corresponding author: steven.herbette@univ-brest.fr*

Abstract

Based on satellite and *in situ* data, the dynamic characteristics and vertical structure of a surface intensified mesoscale dipole recently expelled from the South East Madagascar Current (SEMC) is described for the first time. The dipole was surveyed 250 nautical miles south of Madagascar between 14 and 23 November 2016, during west-east and south-north transects carried out over the northern Madagascar Ridge. The dipole consisted of two counter-rotating vortices of similar size (100 km) and intensity (0.7 f), and an intense southwestward jet (150 cm s^{-1}) in the frontal region between the two eddies. The cyclonic eddy was lying on the western side of the anticyclonic eddy. With azimuthal velocities reaching 100 cm s^{-1} at the surface and decreasing slowly with depth (40 cm s^{-1} at -600 m), this MAD-Ridge dipole was defined as a highly non-linear (Ro~0.7) isolated eddy-type structure ($c\beta$ ~ 11 cm s^{-1} and $U/c\beta$ ~ 0.7) capable of trapping and advecting water masses over large distances. The enhanced concentration of chlorophyll-a found in the cyclone relative to the anticyclone could be tracked back to the spin-up phase of the two eddies and attributed to eddy-pumping. The eddy cores were located above the pycnocline (1026.4 kg m^{-3}), within the upper 600 m, and consisted of varieties of Subtropical Underwater (STUW) found within the SEMC. The STUW found in the anticyclone was more saline and oxygenated than in the cyclone, highlighting mixing with the inshore shelf waters from the southeastern coastal upwelling cell off Madagascar. Observations suggest that the dipole

interacted strongly with the chaotic bathymetry of the region, characterized by a group of five seamounts lying between -240 m and -1200 m. The bathymetry blocked its westward advection, trapping it in the vicinity of the seamount for more than 4 weeks, so enhancing the role of the eddy-induced velocities in stirring the surrounding water masses. Squeezed between the southern Madagascan shelf and the northern flank of the anticyclone, two filament-like dynamic features with very different water-mass properties could be observed on the south-north transect: i) one filament highly concentrated in chlorophyll-*a* demonstrating the capacity of the eddy to export shelf water offshore; ii) intrusions of a more southern-type of STUW generally found south of the South Indian Counter Current (SICC) recirculating on the external flanks of the anticyclone. Although the observed circulation and hydrography were largely constrained by the presence of the mesoscale eddy dipole, unmistakable fine-scale dynamics were also observed in the vicinity of the MAD-Ridge seamount, superimposed onto the mesoscale eddy flow.

1. Introduction

1.1 Context

Seamounts are ubiquitous in the World's Oceans. In recent years, advances in satellite altimetry have allowed >14 000 seamounts with a vertical extension exceeding 1000 m to be spotted (Kitchingman et al., 2007). According to Lavelle and Mohn (2010), >100 000 tall seamounts still remain uncharted as a consequence of limitations in the resolution of satellite altimetry. The proportion of seamounts that have had their environment monitored is also extremely low, even though seamounts are known to play crucial roles in structuring the ecology of the oceans, and more recently, for their vulnerability to human exploitation (Clark et al., 2010; Schlacher et al., 2010). Seamounts are often seen as key habitats for marine life, even more so in oligotrophic waters where they are considered as hotspots for life and biodiversity (Genin and Boehlert, 1985; Dower et al., 1992; Rogers, 1994; Mouriño et al., 2001). In addition, many are located in Areas Beyond National Jurisdiction (ABNJ) where there is little regulation, leaving them targeted by industrial fisheries (Marsac et al., 2020) and sometimes resulting in the total collapse of the fishery (Koslow, 1997; Clark, 2001; Pitcher et al., 2010).

There seems to be general consensus in the literature that the associated with seamounts are linked tightly to the dynamics of oceanic circulation. At least two of today's general concepts arose in the literature of the 1980s and 1990s, when interest in seamount biology started to rise. The first states that there is increased primary productivity and chlorophyll-*a*

(hereafter chl-*a*) around seamounts because of the enhanced vertical flux of nutrients towards the euphotic layer. The second is that currents around seamounts favour the retention of organic matter and organisms, which contributes to the specificity of the ecosystems, isolated from the surrounding environment, and sheltering a restricted and unique biodiversity (Genin and Boehlert, 1985; Dower et al., 1992; Boehlert and Mundy, 1993; Comeau et al., 1995; Mouriño et al., 2001; Genin, 2004). However, there has been little tangible evidence to sustain these concepts (Genin and Dower, 2007; Rowden et al., 2010).

1.2 Influence of seamounts on the ocean circulation

Theoretical and idealized modelling has helped in understanding the physical processes at play when a tidal or non-tidal flow encounters an isolated seamount. For instance, Garrett (2003) found that steep seamounts, located in areas of strong tidal flow, act as stirring rods for the ocean where the energy from lunar and solar barotropic tides is converted into an internal wave field, commonly referred to as the internal (baroclinic) tide. Internal waves then propagate into the ocean interior inducing motions of the density surfaces (isopycnals). Whether this internal wave field breaks locally or far away, such dissipation generates sites of intense vertical turbulent mixing that contribute to the local stratification and nutrient enrichment of surface layers. Non-tidal flows impinging on a seamount may also generate internal waves, commonly referred to as Lee waves. The latter will also either dissipate locally or radiate away depending on the characteristics of the flow and the topography (Nikurashin and Ferrari, 2010). When the non-tidal flow is characterized by low Rossby numbers, it will deviate anticyclonically around the seamount. In some conditions, this anticyclonic flow may even remain trapped over an obstacle, constituting a feature known as a Taylor cap (or Taylor column; Huppert, 1975). The formation of a Taylor column is also accompanied by the detachment of a cyclonic eddy that may remain trapped in the vicinity of the obstacle or advected away (Huppert and Bryan, 1976; Royer, 1978; Verron and Le Provost, 1985; Herbette et al., 2003). Oceanic currents induced by intense mesoscale eddies enter this category of non-tidal flows. Taylor caps can produce large uplift of the interior isopycnals (Dower and Mackas, 1996), which could enhance phytoplankton blooms. They can also be long-life features facilitating the retention of particles and biota near the seamount summit (Mullineaux and Mills, 1997).

1.3 The northern Madagascar Ridge

In the South West Indian Ocean (SWIO), the 1500-km long Madagascar Ridge is an elongated aseismic plateau that extends from the tip of the southern Madagascar shelf all the way down to 35°S (Sinha et al., 1981). It separates the Mozambique and Madagascar basins, two ocean basins of mid- to late Cretaceous age, and typically rises from abyssal depths (-5000 m) to between 1500 and 2500 m of the sea surface (Fig. 1). On its southern portion (at 33°12'S), the Walters Shoal, a seamount almost reaching the sea surface, is its most prominent feature. On its northern portion, just south of the Madagascan shelf, the ridge widens and becomes a rough plateau composed of at least five seamounts, which have never been monitored.

The northern Madagascar Ridge is a productive region of highly complex and turbulent dynamics. It is influenced by cold filaments, highly concentrated in chl-*a*, detaching from the adjacent southern Madagascar coastal upwelling cells (Lutjeharms and Machu, 2000; Quartly, 2006; Quartly et al., 2006; Ramanantsoa et al., 2018; Demarcq et al., 2020). It is also located in the very energetic retroflection region of the South East Madagascar Current (SEMC) (Pous et al., 2014; Vianello et al., 2020), which flows south along the east coast of Madagascar, transporting around 35 Sv[1] of warm, saline water from the subtropical South Indian Ocean (Siedler et al., 2009). It originates from the bifurcation, at 20°S, of the Indian Ocean South Equatorial Current (SEC) (DiMarco et al., 2002) and forms the northern part of the western boundary current of the South Indian Ocean subtropical gyre. At the southern tip of Madagascar, the dynamics of the SEMC becomes highly complex with three possible modes (Quartly et al., 2006; Ramanantsoa et al., 2020): i) an early retroflection mode in which the SEMC veers eastwards several hundreds of kilometres north of the southern tip of Madagascar (~23°S); ii) a canonical retroflection mode in which the SEMC overshoots the southern tip of Madagascar, flowing south, before finally veering east; iii) a third mode in which the SEMC continues to flow west following the southern Madagascan shelf edge. The last two modes contribute to the formation of intense mesoscale eddies or dipoles that propagate westwards over the Madagascar Ridge and towards the Agulhas Current (De Ruijter et al., 2004; Nauw et al., 2008; Siedler et al., 2009; Halo et al. 2014). Ridderinkhof et al. (2013) showed that, south of Madagascar, these mesoscale eddies often take the form of large dipoles, among which some may remain strong enough to subsequently trigger an early retroflection of the Agulhas Current.

[1] Sverdrup (Sv) = 10^6 m^3 s^{-1}

1.4 Previous cruises on the northern Madagascar Ridge

A few research cruises had previously taken place over the northern Madagascar Ridge. In 2001, the ACSEX hydrographic cruise (Agulhas Current Sources Experiment) consisted of four transects perpendicular to the Madagascar shelf that captured the SEMC as well as an anticyclonic and cyclonic eddy dipole (De Ruijter et al., 2004; Nauw et al., 2008). In 2005, the Madagascar Experiment (MadEx) highlighted the presence of intensified currents at all depths of the water column (Quartly, 2006; Quartly et al., 2006). In September 2008, eight across-shore transects carried out on board the RV *Dr Fridtjof Nansen* along the eastern Madagascan coast, emphasized the complex dynamics of the northern and southern branches of the East Madagascar Current (Voldsund et al., 2017). One year later, the same vessel returned to the area and surveyed the south and west coasts of Madagascar within the framework of the Agulhas Somali Large Marine Ecosystem (ASCLME) programme (Pripp et al., 2014). Evidence of coastal upwelling was found along the southeast coast of Madagascar and at two sites on its west coast, Cap Saint André and Nosy Be Island (Alvheim et al., 2009). In November/December 2009, a multidisciplinary cruise was conducted over a group of seamounts of the SWIO, whose summits lay at depths situated between -100 m and -1250 m. The objective of that programme was to gain knowledge on the pelagic ecosystems around the seamounts and to determine the dominant physical processes at play (Read and Pollard, 2017). Five of the seamounts were located over the South West Indian Ridge and one over the southern Madagascar Ridge, close to the Walters Shoal (Rogers, 2016). Results showed that oceanic currents around the seamounts were linked to the internal wave field originating from the tidal flow, or to the presence of mesoscale eddies. Although Taylor caps were detected at a few locations during that survey (Pollard and Read, 2017), their existence was intermittent and did not influence the observed circulation and hydrography.

1.5 The MADRidge project

In 2016/2017, an international programme (the MADRidge project) was designed to monitor the ecosystems in the vicinity of shallow seamounts in the SWIO (Fig. 1). The International Union for Conservation of Nature (IUCN) and the French Institut de Recherche pour le Développement (IRD), together with partners in France, South Africa and Madagascar, carried out three multidisciplinary research cruises that surveyed three shallow seamounts lying in three very different dynamic environments (Roberts et al., 2020). The study describes the physical (currents and hydrography) and biogeochemical (oxygen and fluorescence) *in situ* data collected during the MAD-Ridge Leg 1 expedition that focused only

on one of the three seamounts: an unnamed seamount, thereafter named MAD-Ridge, located on the northern Madagascar Ridge. The work here aims at providing knowledge of the underlying dynamics within this very turbulent environment, focusing specifically on the role of the bathymetry in constraining the circulation and hydrography. The *in situ* survey offered an unique opportunity to characterize in detail a surface-intensified mesoscale eddy dipole that had been freshly expelled from the SEMC and stayed trapped in the vicinity of the MAD-Ridge seamount during the whole cruise. Our objectives are to describe in detail the synoptic conditions in place during the MAD-Ridge Leg 1 cruise and to analyse how the conditions may have influenced the nature of the flow-topography interactions and the environmental response in term of chl-*a* concentration.

1.6 Outline

Section 2 below describes the MAD-Ridge Leg 1 cruise, focusing on the vertical profiling of the physical (currents and hydrography) and biogeochemical (oxygen and fluorescence) *in situ* data, and their subsequent validation and calibration. The satellite data (sea surface height and chl-*a*) and the methods used to track mesoscale eddies in the region are also briefly explained. Section 3 then highlights the presence during the survey of a surface-intensified coherent mesoscale cyclonic/anticyclonic dipole expelled from the SEMC. The vertical structure of the dipole is characterized in terms of velocities, water mass properties and its impact on the vertical distribution of chl-*a* and nutrients. Fine-scale turbulent dynamic features such as filaments, which superimpose onto the dominant flow induced by the mesoscale eddy dipole, are described in Section 4. The observations are discussed in Section 5 in the light of theoretical work on eddy-seamount interactions and recent progress in the understanding of the variability of the SEMC. Finally, Section 6 summarizes our observations and discusses the important role played by the northern Madagascar Ridge in Global Ocean circulation by governing aspects of connectivity between the SEMC and the Agulhas Current.

2. Data and Methods

2.1 The MAD-Ridge cruise

The MAD-Ridge Leg 1 cruise took place between 8 and 25 November 2016 (doi: 10.17600/16004800) on board the RV *Antea*. It focused on the MAD-Ridge seamount at 27°29'S, 46°16'E. The cruise consisted of two perpendicular transects of ~150 nautical miles that crossed the summit of the seamount (Fig. 2). The west-east transect was carried out

during the period 14-18 November, and the south-north transect from 19 to 23 November. Each station along the transects consisted of conductivity-temperature-depth (CTD) and lowered acoustic Doppler current profiler (L-ADCP) vertical profiling down to -1000 m. Stations were every 15 nautical miles outwards from the seamount, and at intervals reduced to 5 nautical miles over the slopes and summit of the seamount. The west-east transect (45°-47°30'E, at 27°30'S) had 15 stations, the south-north transect (28°17'S - 25°40'S, at 46°15'E) 16 stations. The northernmost station of the meridional transect was located on the outer edge of the southern Madagascan continental shelf on the -840 m isobath. Ship acoustic Doppler current profiler (S-ADCP) measurements were collected along the whole cruise track.

2.2 CTD and nutrients data

In situ vertical profiles of temperature, salinity, dissolved oxygen and fluorescence were collected using a Seabird SBE 911+ CTD-O_2 equipped with a Wetlabs ECO FL fluorometer. The CTD-O_2 probe had two sensors for temperature, salinity and dissolved oxygen. The vertical profiles were made from the surface to 1000 m. Seawater samples were collected at different depths (up to 11 samples per cast) to calibrate the salinity (measured on board using a Portasal salinometer and OSIL normal seawater), oxygen (measured on board using the Winkler method) and fluorescence (filtration on board and phytoplankton pigment analysis at the laboratory using High Pressure Liquid Chromatography) sensors. Nutrients (NO_2, NO_3, PO_4 and $Si(OH)_4$) were determined by the classical colorimetric method (Oudot et al., 1998) on samples collected at each station. CTD-O_2 calibration was performed using the CADYHAC software from IFREMER (Kermabon et al., 2015). Conservative temperature and absolute salinity were calculated according to the TEOS-10 equations, and the vertical stretching term of the potential vorticity (PV) was derived as $|f|N^2/g$, with f the Coriolis parameter, N the Brunt-Väisälä frequency and g the constant for gravity (Talley et al., 2011).

2.3 In situ current measurements

The RV *Antea* has a 75 kHz RDI Ocean Surveyor hull mounted S-ADCP, which allows for continuous vertical profiling of the ocean currents along the ship's track. Velocity components were time-averaged over 2 min. The vertical resolution (bin size) was set to 16 m, with a maximum measurement depth down to -600 m. The S-ADCP data were processed using the CASCADE software from IFREMER (Le Bot et al., 2011). A tidal correction was applied using the TPX08-atlas (Egbert et al., 2002). The final S-ADCP product consisted of a

2-km horizontal resolution set of vertical profiles for the zonal *u* and meridional *v* components of the velocity vector.

Two 300 kHz RDI Workhorse (upward and downward orientated) L-ADCPs were attached to the CTD frame to measure the zonal and meridional components of the velocity through the water column at each CTD station, with an 8 m vertical bin-size resolution. L-ADCP data were processed on board, then calibrated after the cruise using a software developed by IFM-GEOMAR/LDEO (Thurnherr, 2014). The L-ADCP failed at stations 2 and 3. Despite the coarser horizontal resolution of the L-ADCP sampling (~25 km for the L-ADCP vs. 2 km for the S-ADCP), the vertical structure of the velocity fields given by the S-ADCP and L-ADCP were similar (Supplementary material Fig. S1). Hence, the S-ADCP data are used in the analysis.

2.4 Altimetry data

Daily interpolated merged delayed time altimetry data gridded at ¼° resolution, produced by Ssalto/Duacs and distributed by the Copernicus Marine Environment Monitoring Service (CMEMS, http://marine.copernicus.eu/) were used to describe the surface mesoscale synoptic conditions over the northern Madagascar ridge. Mean Eddy Kinetic Energy (EKE) was derived from Sea Level Anomaly (SLA) data over a large portion the SWIO (Fig. 1) as follows:

$$\overline{EKE} = \frac{1}{2}\left(\overline{u_{gs}'^2} + \overline{v_{gs}'^2}\right), (1)$$

where u'_{gs} and v'_{gs} are the zonal and meridional components of the surface geostrophic current anomaly, and the $\bar{.}$ stand for a linear time average operator from 1995 to 2015. Further, Absolute Dynamic Topography (MADT) data were used to compute the absolute surface geostrophic currents, relative vorticity and the Okubo-Weiss quantity[2] (Okubo, 1970; Weiss, 1991).

*2.5 Ocean surface colour and chl-*a *satellite data*

Daily 4-km resolution MODIS ocean colour data provided by NASA (https://oceancolor.gsfc.nasa.gov/) were processed to produce composite 3-day images of the chl-*a* surface distribution.

[2] The Okubo-Weiss quantity λ_{ok} measures the local influences of the shear/strain rate against the relative vorticity. It is calculated by subtracting the relative vorticity $\zeta = (\partial_x v_{gs} - \partial_y u_{gs})^2$ from the deformation rate $\sigma = (\partial_x u_{gs} - \partial_y v_{gs})^2 + (\partial_x v_{gs} + \partial_y u_{gs})^2$: $\lambda_{ok} = \sigma^2 - \zeta^2$.

265

266 *2.6 Eddy tracking and dipole occurrence*

267 Seven-day SLA products at ¼° resolution were used to monitor the long-term eddy activity
268 in the region over the period 1993-2016 and to infer statistics on the presence of surface-
269 intensified mesoscale eddy dipoles in the region. Eddies were tracked using the algorithm
270 developed by Chelton et al. (2007). The method consists of finding SLA extrema sitting
271 inside closed SLA contours (Chelton et al., 2007; Mason et al., 2011; Halo et al., 2014). Once
272 an eddy is identified, the eddy centre coordinates are recorded. The method was further
273 adapted to: i) discard weak eddies that have SLA extrema <10 cm in amplitude; ii) only retain
274 eddies potentially interacting with the seamount – the typical eddy radius in the area being 90
275 km [Halo et al., 2014], eddies found farther from the seamount summit were discarded; iii)
276 distinguish single eddies from dipoles. Dipoles were diagnosed when a cyclone and an
277 anticyclone could both be observed during the same 7-day period, <180 km from the
278 seamount summit, and when the maximum velocity in the frontal region between the two
279 eddies was at least 1.5× the velocity found on the eddy periphery. For each dipole detected, a
280 "dipole strength" (DS) was computed as an estimate of the gradient of SLA in the frontal
281 region, subtracting the minimum SLA found within the cyclone (SLA_{min}) from the maximum
282 SLA found within the anticyclone (SLA_{max}) and dividing the difference by the distance
283 between the two eddy centres ($d_{c/ac}$): $DS = (SLA_{max} - SLA_{min}) / (d_{c/ac})$.

284

285 *2.7 Bathymetry*

286 The bathymetry of the MAD-Ridge seamount was surveyed on board using the two single-
287 beam echo-sounders (12 and 38 kHz) mounted on the RV *Antea*. The echo-sounder
288 measurements differed significantly from the ETOPO 1[3] and GEBCO 30[4] products based on
289 satellite altimetry. The MAD-Ridge seamount summit was indeed found 6 km farther south
290 than expected. In addition, although the seamount reached the sea surface in ETOPO 1 and
291 GEBCO 30, it was found at -240 m during the cruise. The SRTM[5] (Shuttle Radar Topography
292 Mission) bathymetry product which showed the seamount at the correct position just 150 m
293 below the sea surface, is used in the following for displaying the bathymetry of the area.

294 According to the *in situ* data, the seamount summit consists of a 20-km wide oval plateau,
295 slightly elongated along a south-north axis, that plunges steeply from -240 m to the seafloor at

[3] ETOPO 1 : doi:10.7289/V5C8276M
[4] GEBCO 30: doi:10.5285/a29c5465-b138-234d-e053-6c86abc040b9)
[5] SRTM: https://topex.ucsd.edu/WWW_html/srtm30_plus.html

-1600 m (Fig. 2). It should be stressed that the MAD-Ridge seamount is not an isolated structure; it is surrounded by four deeper summits situated between -600 m and -1200 m. The detailed topography of these neighbouring seamounts was not monitored during the cruise.

2.8 In situ *geostrophic velocities*

The components of the geostrophic velocity perpendicular to the west-east and south-north transects were calculated integrating vertically the thermal wind equation:

$$\frac{\partial v_{\perp}}{\partial p} = \frac{-1}{f}\frac{1}{\Delta x_{//}}\Delta\left(\frac{1}{\rho}\right). \quad (3)$$

$v_{\perp}$ is the component of the geostrophic velocity perpendicular to each segment separating two CTD vertical profiles, p the pressure, f the Coriolis parameter, $\Delta x_{//}$ the segment length and $\Delta\left(\frac{1}{\rho}\right)$ the variation of specific volume over the segment. The right side of Eq. (3) was computed from the TEOS-10 Gibbs equation of state using conservative temperature and absolute salinity. Eq. (3) was then integrated vertically from a pressure of reference. This pressure of reference was calculated for each segment as the pressure at which the vertical shear of the S-ADCP velocity component perpendicular to the segment balanced the right-side term of Eq. (3). A horizontal low-pass Lanczos filter was applied to both the S-ADCP and temperature and salinity data prior to the integration, to remove spurious signal associated with non-geostrophic dynamics. The cut-off wave number was set to 1/20 km^{-1}, a value ~3 times less than the Rossby radius of deformation found in the region (Chelton et al., 1998). Ageostrophic velocities were calculated by subtracting the calculated geostrophic velocities from the non-filtered S-ADCP velocity data.

3. Characteristics of a strong surface intensified mesoscale eddy dipole

A map of surface EKE, a proxy for mesoscale turbulence in the ocean, provides robust evidence that the MAD-Ridge seamount is located in a region characterized by a high level of turbulent mesoscale activity, with EKE values ranging between 630 and 800 cm^2 s^{-2} (Fig. 1). Although such levels of EKE are about 3× less than those found in the most energetic western boundary current systems (Pilo et al., 2015), they are higher than in most parts of the ocean and suggest the presence of highly variable synoptic conditions.

3.1 Surface signature and coherence of the mesoscale eddy dipole

The cruise took place when a surface-intensified anticyclonic/cyclonic eddy dipole was present over the northern Madagascar Ridge (Fig. 3). The anticyclone was centred over the seamount, with its cyclonic counterpart lying on its western flank. Both eddies were roughly the same size, with a radius of approximately 100 km, and of similar amplitude. Within the anticyclone, the maximum values of SLA and surface relative vorticity were >35 cm (Fig. 3) and of the order of -0.7 f (f ~ -6.6 × 10^{-5} s^{-1}) (Fig. 4). Similar but opposite values were found within the cyclone, with minimum values of SLA below -35 cm and surface relative vorticity of the order of +0.7 f. The frontal region between the two eddies was characterized by intense southwestward geostrophic jet-sustaining velocities >150 cm s^{-1} (Fig. 3), which highlights the extreme intensity of the mesoscale dipole. Using an eddy-tracking algorithm, the vortices could be traced back to 26 October 2016, coinciding with the time when the SEMC started to subdivide into two branches as seen in the surface relative vorticity maps (Fig. 4). The west-flowing branch followed the shelf edge, whereas the southwest-flowing branch detached itself from the coast at 25°S, 47°E. The southward flow was observed until 27°S, where the SEMC started to veer westwards. Cyclonic vorticity developed on the inshore side of the current, and anticyclonic vorticity strengthened on the offshore side. On 2 November 2016, the dipole was fully formed, although it was still embedded within the SEMC. While strengthening, it detached itself from the SEMC and propagated southwest towards the MAD-Ridge seamount. From 9 to 23 November 2016, the southwestward propagation of the dipole slowed, and the dipole stayed in the vicinity of the seamount for two full weeks. By 30 November, the cyclonic eddy had moved slightly southwest and the anticyclone had elongated notably in a northeast-southwest direction. Another cyclonic eddy could be observed on the eastern flank of the anticyclone. On 7 December 2016, the anticyclone split into two eddies. One stayed trapped over the seamount, but the most intense one continued to form a dipole with the original cyclone. The dipole then accelerated its southwestward propagation. It was tracked until 24 December 2016 (not shown) when both eddies finally dissipated, and another similar dipole began to interact with the MAD-Ridge seamount. Hence, the west-east and south-north transects of Leg 1 provided a unique opportunity to survey a strong mesoscale eddy dipole freshly expelled from the SEMC and interacting with the northern Madagascar Ridge.

3.2 Vertical structure of the mesoscale eddy dipole: focus on azimuthal velocities

The ship-mounted S-ADCP measurements provide additional information on the vertical structure of the currents within the dipole. The west-east transect crossed the entire anticyclonic eddy through its centre and captured the southeastern portion of the cyclone (Fig.

3). The agreement between the low-pass spatially filtered S-ADCP currents and the surface geostrophic currents derived from altimetry shows that the dipole is accurately located by the altimetry (Fig. 3), and lends confidence in the ability of the low-pass Lanczos filter to retrieve the geostrophic part of the currents from the S-ADCP data. The vertical structure of the flow confirms that the dipole was surface-intensified (Fig. 5). Down to -400 m, the mesoscale circulation was in total accord with the existence of the mesoscale eddy dipole: clockwise and anticlockwise circulations were observed within the cyclone and anticyclone, respectively. The highest velocities were found in the southwestward jet that lay within the frontal region between the two eddies (stations 5 and 6), with values above 150 cm s^{-1} at the surface and still as high as 70 cm s^{-1} at -600 m. On the flanks of the dipole, velocities were slightly slower, but still as high as 100 cm s^{-1} in the upper 100 m of the water column, and of the order of 70 cm s^{-1} at - 400 m (Fig. 5a, c, e).

Between the two transects, the anticyclone moved above the seamount while being stretched along a southeast-northwest axis (Supplementary Fig. S2). Hence, the south-north transect only captured one arc of the anticyclonic eddy in which the flow was mostly to the southwest, with velocities of the order of 80–100 cm s^{-1}. Nevertheless, south of 27°S, the flow veered anticlockwise to the east, confirming the anticyclonic rotation. Subsurface velocities were also weaker, not exceeding 40 cm s^{-1} below -400 m. Geostrophic velocities computed from the vertical profiling of density confirm this overall circulation pattern (Fig. 6).

3.3 Vertical structure of the mesoscale eddy dipole: focus on the hydrography

Additional characteristics on the vertical structure of the two eddies is provided by the *in situ* temperature, salinity, oxygen and chl-*a* data collected during the two transects (Fig. 7 and 8). The vertical stretching term of the potential vorticity highlights the squeezing and stretching of the isopycnals and provides extra information on the process of formation of a water mass (Talley et al., 2011).

The doming of the isopycnals (black contours) in Fig. 7 and 8 allows accurate location of the core of the anticyclone (X1) and the southern flank of the cyclone (X2). Considering the average vertical density profile found in the MAD-Ridge region, the 1026.4 kg m^{-3} isopycnal was hereafter selected as the pycnocline that separates the surface stratified waters from the slightly deeper non-stratified waters ($N^2 < 10^{-4}$ s^{-2}). On the west-east transect, the curvature of this pycnocline clearly showed the presence of a surface-intensified mesoscale eddy dipole. This isopycnal depth is found at -400 m within the anticyclone, and at -300 m within the cyclone (Fig. 7). The south-north transect only intersected the southwestern portion of the

anticyclone. At stations 17, 18 and 19 (south of the seamount), the depth of the pycnocline was similar to that (-400 m) observed within the anticyclone on the west-east transect (stations 11–15). The rise of the pycnocline north of the seamount and adjacent to the southern Madagascan shelf edge is in accord with the intensified westward flow observed on the northern flank of the anticyclone (Fig. 8).

The cores of these two eddies were located above the pycnocline. At such depths, azimuthal velocities are at their highest (Fig. 5 and 6), and the water mass properties differed substantially whether they belonged to the anticyclone (X1), cyclone (X2) or the frontal zone between the two eddies (Fig. 7). Surface waters found within the cyclonic eddy were on average 0.6°C cooler and 0.1 g kg^{-1} more saline than those within the anticyclonic eddy. This difference is even more visible when considering the salinity maximum centred on the 1026.0 kg m^{-3} isopycnal: the salinity was 0.3 g kg^{-1} higher in the anticyclone (36 g kg^{-1} at stations 13, 14 and 24) than in the cyclone.

3.4 Water mass properties within the mesoscale eddy dipole

Water mass properties can be investigated by plotting the CTD vertical profiles on two diagrams, conservative temperature (CT) vs. absolute salinity (SA) (Fig. 9a, b) and conservative temperature vs. dissolved oxygen (O_2) (Fig. 9c). Profiles are grouped into three classes, depending on whether they were collected within the cyclonic eddy, within the anticyclonic eddy or within the frontal zone in between the two eddies. This classification was made using altimetry data.

3.4.1 Below the pycnocline, within the depth range of Antarctic Intermediate Water (AAIW):

Between -800 m and -1000 m, for waters heavier than 1027.0 kg m^{-3}, the signature of AAIW is clearly visible (Fig. 9a, b), with a minimum in salinity falling below 34.6 g kg^{-1} and a minimum in temperature <10°C (Emery and Meincke, 1986). These properties match observations carried out within the Agulhas Current, confirming the widespread nature of this water mass in the SWIO (Beal et al., 2006).

Within this depth range too, the isopycnals were still deflected, mirroring the surface-intensified dipole. However, the fact that all datapoints reported on the CT/SA and CT/O_2 diagrams for that depth range are superimposed, independent of their location in the dipole (Fig. 9), is an indication that the isopycnal variations of temperature, salinity and oxygen were weak. The low values of geostrophic velocities (~10 cm s^{-1}) at those depths (Fig. 6) confirm

the belief that these water masses did not belong to the core of the eddies forming the mesoscale eddy dipole, but rather were being entrained by the surface eddy cores.

3.4.2 Below the pycnocline, within the depth range of South Indian Central Water (SICW):

On both transects, just below the eddy core, between the 1026.4 kg m^{-3} and 1026.7 kg m^{-3} isopycnals, South-East Indian Sub-Antarctic Mode water (SEISAMW) was identified on all the vertical CT/SA-profiles (Hanawa and Talley, 2001). Within that depth range, we observed no spatial variation of temperature, salinity or oxygen on any given isopycnal (Fig 9). The characteristics in temperature (10–15°C) and salinity (34.7–35.3 g kg^{-1}) are similar to the heavier range of central waters commonly found within the subtropical gyre of the SWIO (Emery and Meincke, 1986; Sprintall and Tomczak, 1992; Beal et al., 2006). In addition, we observed high oxygen concentration of >200 µmol kg^{-1} (Fig. 9c) and low potential vorticity values (Fig. 7d and 8d). This helps to identify more accurately this water mass as the SEISAMW, a heavy variety of Sub-Antarctic Mode Water (SAMW), formed within the deep-winter mixed layer of the South East Indian Ocean (Hanawa and Talley, 2001). New et al. (2007) have identified SEISAMW over the Mascarene plateau on the southern side of the SEC. These observations suggest that the SEMC transported this water mass, ensuring a connection between the Mascarene plateau and the northern Madagascar Ridge.

3.4.3 Above the pycnocline, within the depths range of South Tropical Underwater (STUW) and Tropical Surface Water (TSW)

The STUW, characterized by salinity >35.5 g kg^{-1} and a high potential vorticity of ~150 × 10^{-11} s^{-1} (Hanawa and Talley 2001; Nauw et al., 2006), can be seen in all the MAD-Ridge CTD profiles above the pycnocline between the 1026.4 and 1024.8 kg m^{-3} isopycnals (Fig. 7 and 8) and on the CT/SA diagram (Fig. 9). That water mass constituted the core of both eddies forming the mesoscale eddy dipole. Nevertheless, there was some indication that the anticyclonic eddy core (X1 in Fig. 7 and 8) contained less-altered STUW than anywhere else. Indeed, extremely high values of salinity (>36 g kg^{-1}) were observed on the west-east transect at station 13, on 18 November, east of the seamount (X1 in Fig. 7), and then a few days later on 21 November, at stations 23-24 just north of the seamount when the eddy had moved onto the seamount summit (X1 in Fig 8).

We now attempt to backtrack these properties to the formation of the dipole within the SEMC. As already mentioned, maps of surface relative vorticity suggest that the cyclone was generated inshore of the SEMC, whereas the anticyclone was formed on its offshore side (Fig.

462 4). The similarity between the CT/SA profiles inside the cyclonic eddy and those observed on
463 the southern continental shelf of Madagascar during the ASCEX cruise (de Ruijter et al.,
464 2004) adds weight to this assumption. The observed difference in salinity between the two
465 eddies was attributable to an existing cross-shore gradient of salinity within the SEMC itself
466 that can be linked to the water mass properties of the SEC. The latter transports a mixture of
467 Tropical Surface Water (TSW) and Sub-Tropical Surface Water (STSW) west, right across
468 the Indian Ocean, the STSW being much more saline than the former, and on the southern
469 side of the SEC (New et al., 2005, 2007). The densest part of the STSW subducts under the
470 Tropical Front to form some kind of intra-thermocline waters commonly referred as Sub-
471 Tropical Underwater (STUW; O'Connor et al., 2002). This water mass is reported to be about
472 0.2 g kg^{-1} more saline than the TSW. When the SEC flows over the Mascarene plateau, water
473 masses are partially mixed, which smooths out the difference in salinity (New et al., 2007).
474 Nonetheless, water masses on the southern edge of the SEC remain more saline than that on
475 the northern edge. When the SEC splits into two branches, as it approaches Madagascar, its
476 southern part forms the southern branch of the EMC that flows south along the Madagascan
477 coast, known as the SEMC. It is made up of STSW and STUW, but the offshore waters are
478 more saline than the inshore ones. As the SEMC flows south along the eastern Madagascan
479 coast, the offshore entrainment of fresh Madagascan shelf water into the SEMC and its
480 subsequent mixing with the waters within the current reinforce the cross-shore salinity
481 gradient, agreeing with the water masses observed within the eddy cores.
482
483 *3.5 Impact of the mesoscale eddy dipole on chl-a and nutrient distribution*
484 Three-day composite maps of satellite sea surface chl-*a* concentration show enhanced
485 phytoplankton concentration within the cyclone (Fig. 10). This fits with the widely spread
486 paradigm that the uplift of isopycnals within cyclones brings more nutrients into the euphotic
487 layer, enhancing primary production (McGillicuddy et al., 1998; Oschlies and Garçon, 1998;
488 Lévy, 2008). The vertical distribution of chl-*a* along the west-east transect confirms this
489 enhancement in the surface layer, accompanied by an uplift of the Deep Chlorophyll-*a*
490 Maximum (DCM), following the upward doming of the isopycnals induced by the cyclonic
491 eddy (X2 on Fig. 7). The DCM within the cyclone reached 0.40 mg m^{-3} at -55 m at station 3,
492 but only 0.20 mg m^{-3} was measured at -125 m at station 14 in the anticyclone.
493 The daily evolution of satellite chl-*a* concentration within both eddies was calculated over
494 their lifetime, from 27 October to 24 December 2016 (Fig. 11). The corresponding chl-*a*
495 concentration was extracted from the centre of both eddies and smoothed with a 3-day-

window moving average to account for missing data caused by cloud cover. The concentration of chl-*a* within the cyclone clearly increased during the spin-up phase of the eddy when the eddy pumping mechanism that uplifts nutrients towards the euphotic zone is meant to be at its maximum (Lévy, 2008). The concentration then decreased, but still remained higher than within the anticyclone by at least 0.05 mg m^{-3} until mid-December 2016.

Although linking the distributions of nitrates and chl-*a* is beyond the scope of this paper, it is worth mentioning that the vertical distribution of nitrate along the two transects is also clearly constrained by the presence of the dipole (Fig. 12). The 1024.0 kg m^{-3} isopycnal separates the nutrient-depleted surface layers from the nutrient-rich subsurface waters, while following a remarkable, classic eddy shape.

4. Evidence of small-scale turbulence

In addition to the presence of a strong mesoscale eddy dipole, the analysis of the MAD-Ridge Leg 1 dataset reveals a series of indications also of fine-scale turbulent dynamics in the region during the cruise.

4.1 Fine scale undulations of the isopycnals

Fine-scale structures, smoothed out when considering the balanced geostrophic flow (Fig. 6a, b) are clearly visible on the west-east and south-north 2-km horizontal resolution S-ADCP transects (Fig. 5). The most striking example was in the vicinity of the seamount, on its western side during the west-east transect, where a series of upward (stations 5 and 7) and downward (stations 4, 6 and 8) undulations of isopycnal depth can be seen (e.g. X3 in Fig. 7). Deviations are of 30 m magnitude and are greatest at the depth of the seamount (-240 m) for the 1025.5 kg m^{-3} isopycnal. These perturbations have a strong signature (>40 cm s^{-1}) in the non-geostrophic velocity field (Fig. 6c), reinforcing the southward velocity of the flow.

4.2 Sharp horizontal density front within the frontal zone of the dipole

The frontal region that separates the two eddies of the dipole was characterized by sharp horizontal gradients of temperature and salinity in the 150-m-thick surface layer (Fig. 7). On the west-east transect, between stations 4 and 6 and separated by just 35 km, the vessel thermosalinograph, which samples water 2 m below the sea surface, reported a 1°C increase

528 in temperature[6] and a 0.15 g kg^{-1} decrease in salinity[7] over 6 h (not shown). Such variations
529 cannot be explained by the net local surface heat and freshwater fluxes and must therefore be
530 linked to the intrinsic properties of the two eddies, i.e. the presence of warmer, more saline
531 water within the anticyclone than in the cyclone. Theoretical studies predict that non-linear
532 processes associated with a turbulent mesoscale eddy field can lead to the enhancement of a
533 pre-existing horizontal density gradient within the surface mixed layer, and in turn generate
534 sub-mesoscale ageostrophic instabilities and strong vertical velocities (McWilliams, 2016).
535 The coarse resolution of the CTD casts during the two transects does not allow any diagnosis
536 of frontogenesis (Capet et al., 2008) nor vertical velocities though inversion of the ω-equation
537 (Pollard and Regier, 1992; Legal et al., 2007; Rousselet et al., 2019). However, the frontal
538 region between the two eddies showed high positive values of the Okubo-Weiss quantity, of
539 the order of 1.7×10^{-10} s^{-2}, a marker for areas characterized by growth of horizontal tracer
540 gradient (Okubo, 1970; Weiss, 1991).
541
542 *4.3 Vertical tilting of the anticyclonic eddy*
543 The anticyclonic eddy was not made of a homogeneous positive vorticity core when the
544 west-east transect (14–18 November 2016) was sampled (Fig. 4). On 16 November 2016,
545 several poles of positive vorticity were seen within the +20 cm SLA, used here to identify the
546 boundary of the anticyclone. According to altimetry, the second part of the west-east transect
547 crossed two of these poles (Fig. 4). One was centred on the seamount summit at stations 7, 8
548 and 9 on 16 November whereas the other one coincided with a maximum of salinity noted
549 farther west at stations 13, 14 and 15 on 18 November. The downward doming of the
550 pycnocline (1026.4 kg m^{-3}) observed at those stations confirms this picture (Fig. 7). A close
551 look at the vertical structure of the isopycnals along this west-east transect reveals that the
552 anticyclone was slightly tilted vertically towards the west, with deeper isopycnals below the
553 eastern pole at station 13 than below the western pole at station 8.
554
555 *4.4 Entrainment of southern STUW waters*
556 The CT/SA and CT/O_2 diagrams (Fig. 9) show that, at station 28 (black dots), the
557 properties of the subsurface water corresponding to the isotherms 17–22°C (between -250 m
558 and -100 m) differed significantly relative to any of the other stations sampled. These
559 subsurface water masses were 0.2 g kg^{-1} more saline and 40 µmol kg^{-1} more oxygenated than

[6] The temperature increases from 23.8°C to 24.8°C.
[7] The salinity decreases from 35.35 g kg^{-1} to 35.2 g kg^{-1}.

the other stations. The DCM (Fig. 8) was also weaker and deeper (0.30 mg m^{-3} at -133 m) than at the two neighbouring stations on either side, just 15 miles away. Station 29 to the north had a DCM of 0.80 mg m^{-3} at -50 m, whereas station 27 to the south had a DCM of 0.35 mg m^{-3} at -80 m. The World Ocean Atlas annual climatology (WOA18) shows that such type of more saline and more oxygenated STUW is found south of the South Indian Counter Current (SICC) between 30°S and 35°S. This more southern type of STUW was also observed near the MAD-Ridge area, in a cross-shore transect carried out off the eastern Madagascan shelf at 25°N in 2008 (Voldsund et al., 2017, their Fig. 8 and 9). Its presence was identified 200 km offshore, beyond the SEMC, within a northward flow of southern waters. The location of station 28 beyond the northern edge of the anticyclone but south of the southern Madagascan slope, in a narrow region of strong westward velocity (Fig. 3), suggests that a filament of this southern type STUW was entrained there by the anticyclonic flow.

4.5 *Detachment of coastal filaments with high surface chl-a content*

The 3-day composite image of chl-*a* for 20–22 November 2016 (Fig. 10) shows that a patch of water highly concentrated in chl-*a* was sampled at stations 29, 30 and 31 during the south-north transect (red line). The elongated, filament-like shape of this patch, along with the evolution of the absolute surface geostrophic velocities in the area (Fig. S2), suggest that it was torn off from the enriched coastal shelf waters of the South-East Madagascar coastal upwelling cell (Ramanantsoa et al., 2018), then advected onto the northern Madagascar Ridge. *In situ* data show indeed that the DCM was stronger and shallower than at any other station of the survey (0.74 mg m^{-3} at -73 m at station 31; Fig. 8).

5. Discussion

Based on satellite and *in situ* data, we have described for the first time the dynamic characteristics and vertical structure of a surface-intensified mesoscale dipole recently expelled from the SEMC (Fig. 1 and 2). The dipole consisted of two counter-rotating vortices of similar size (100 km) and intensity (0.7 f), and an intense southwestward jet (150 cm s^{-1}) lying in the frontal region between the two eddies (Fig. 3 and 4). CTD and S-ADCP vertical profiling revealed that the cores of the two eddies forming the dipole were located above the 1026.4 kg m^{-3} isopycnal, within the upper 600 m (Fig. 5, 6, 7 and 8). Observations also provide evidence that, close to the seamount, fine-scale dynamics superimpose onto the mesoscale eddy field.

5.1 Overall circulation and hydrography: the dominant role of the mesoscale eddy

A non-linear isolated eddy-type structure has the strength to remain coherent over an extended life, trapping water masses within its core and advecting them over long distances (McWilliams and Flierl, 1979; Chelton et al., 2007). Eddies associated with high Rossby number[8] (Ro>0.1) are generally considered non-linear. They may also be defined as isolated when their azimuthal velocities decrease faster than $1/r$ (r being the distance to the eddy centre) away from their core (Morel and McWilliams, 1997). Obtaining a reliably accurate estimate of the azimuthal velocity according to r is usually difficult because of coarse resolution in the observations, background noise, and the fact that eddies are rarely observed as purely axisymmetric features, but rather elongated deformed shapes. A cruder but more reliable estimation of the capacity of an eddy to trap water masses was proposed by Chelton et al. (2007) and relies on its ability to resist dispersion into planetary Rossby waves. This ability may be measured by the ratio of the maximum azimuthal velocity (U) over the eddy propagation speed ($c\beta$). The eddy propagation speed is here estimated as the zonal phase speed of planetary Rossby waves $c\beta = \beta R_d^2$, with $R_d = NH/|f|$ the Rossby deformation radius, N the Brünt-Väisälä frequency, and β the meridional gradient of the Coriolis parameter f (Sutyrin and Morel, 1997). With maximum relative vorticity values of the order of $0.7\,|f|$, azimuthal velocities >70 cm s^{-1} within the upper 600 m layer and a stratification of the order of $N^2 \sim 7\times10^{-5}$ s^{-2}, the MAD-Ridge dipole classifies itself as a highly non-linear isolated eddy-type structure ($c\beta \sim 11$ cm s^{-1} and $U/c\beta \sim 0.7$).

Hence, during the MAD-Ridge Leg 1 cruise, the circulation, hydrography and primary production over the northern Madagascar Ridge were largely dominated by the signature of a surface-intensified mesoscale eddy feature. The water masses found within the cyclonic and anticyclonic eddy cores corresponded to the water masses at the formation site, i.e. a mixture of coastal upwelled waters from the southeastern Madagascar upwelling cell and STUW found within the SEMC. In addition, the distribution of chl-*a* within the dipole was originally generated during the spin-up phase of the two eddies. Upward eddy pumping within the cyclonic eddy led to enhanced primary production, which was then advected by the dipole onto the ridge (Fig. 10).

However, our study shows that these dipoles were more than just intense and long-life coherent structures. The strong induced velocities also entrained and stirred the surrounding

[8] The Rossby number $Ro = U/(|f|L)$ is a non-dimensional parameter computed as the ratio of the non-linear terms of the momentum equations over the Coriolis terms. For an eddy-like structure, U and L correspond to the eddy radius and the maximum azimuthal velocity, respectively. The ratio U/L is sometimes replaced by the maximum relative vorticity in the eddy core.

625 wates masses. Chl-*a* patches were torn off from the South East Madagascar coastal upwelling
626 cell onto the northern Madagascar Ridge, along with intrusions of nearby southern
627 Madagascan shelf waters originating from south of the SICC.
628
629 *5.2 Influence of the bathymetry on the eddy flow*
630 The mesoscale eddy-dipole was observed in the vicinity of a tall and shallow seamount,
631 whose summit lies 240 m below the sea surface within the isopycnal layer where the cores of
632 the eddies resided. Therefore, the dynamics and evolution of the dipole would be expected to
633 be strongly influenced by the seamount, and more generally by the chaotic bathymetry of the
634 northern Madagascar Ridge, itself made up of several seamounts lying between -1200 m and -
635 240 m (Fig. 2). A series of observations, described below, support this hypothesis.
636 Surface-intensified mesoscale eddies typically self-propagate westwards at the zonal phase
637 speed of the planetary Rossby waves, and dipoles can even propagate faster because of their
638 mutual advecting effect (Hogg and Stommel, 1985). In the absence of bathymetry, the
639 mesoscale eddy dipole should have therefore been moving west at a speed >10 km day^{-1}.
640 However, it remained trapped in the vicinity of the seamount for more than 4 weeks. Only an
641 eastward barotropic flow or some topography-induced effect could have in theory inhibited
642 the westward propagation of the eddy (Morel, 1995; Vandermeirsch et al., 2001). Hence, in
643 the absence of the former, the dynamic influence of the topography must be responsible for
644 the trapping of the eddy above the seamount. A seamount may in fact slow down the
645 propagation of an eddy (Herbette et al., 2003). In the presence of chaotic topography, eddies
646 can even remain trapped in the area for several weeks (Richardson and Tychensky, 1998;
647 Herbette, 2003; Sutyrin et al., 2011).
648 The interaction of a mesoscale eddy with a seamount favours its erosion through
649 filamentation and may lead to its vertical or horizontal splitting (Herbette et al., 2003, 2005).
650 Erosion is always accompanied by the deformation of the vortex, and results from an external
651 shear induced by the formation of two extra vortices, a cyclone that detaches from the
652 seamount and an anticyclone that forms over the seamount as a Taylor cap (Herbette et al.,
653 2003). Maps of surface relative vorticity show that the shape of the mesoscale eddy dipole
654 kept evolving during the cruise. The anticyclonic eddy was notably deformed between 9 and
655 23 November (Fig. 4), which may have resulted into the multiple poles of positive vorticity
656 observed within the +20 cm SLA closed contour. Differences in the vertical structure of the
657 flow between the two transects also highlighted the evolution of the eddy. The dipole intensity
658 was weaker at depth on the south-north transect than on the west-east transect about 4 days

earlier (Fig. 6). In addition, there was vertical tilting of the dipole vertical structure. These observed deformations are similar to results obtained from idealized simulations of an eddy encountering a seamount (Herbette et al., 2003, 2005; Sutyrin et al., 2011) and tend to support our hypothesis that the dipole studied here was, at a fine scale, influenced by the seamount.

5.3 The northern Madagascar Ridge: a region characterized by highly complex circulation

5.3.1 Mesoscale variability and retroflection of the SEMC

The 1993-2016 time-series of daily SLA allowed us to track the presence of cyclones, anticyclones and dipoles over the northern Madagascar Ridge (Section 2.6 above). Dipoles were found in the area >38% of the time, single cyclones and anticyclones about 25% and 30%, respectively (not shown). Although the strength of the MAD-Ridge dipole ($DS_{MAD\text{-}Ridge}$ = 0.32 cm km^{-1}) was among the strongest of the time-series ($\overline{DS}$ = 0.20 ± 0.06 cm km^{-1} and $DS \in [0.07, 0.50]$ cm km^{-1}), the analysis demonstrates that such surface-intensified dipolar eddies are not exceptional in the area. The northern Madagascar Ridge is in fact characterized by high values of mean EKE. Previous work attributed this intense variability to the passage of intense mesoscale eddies travelling from east to west, coming either from the nearby SEMC or from the SWIO (Quartly et al., 2006; Ridderinkhof et al., 2013; Halo et al., 2014). A recent study based on SLA data showed that much of the variability in circulation in the region was related to three retroflection regimes of the SEMC (Ponsoni et al., 2016; Ramanantsoa et al., 2020). A preliminary analysis of a 2-year current-meter time-series from two moorings deployed on the eastern and western flanks of the MAD-Ridge seamount confirmed that the variability of the circulation over the northern Madagascar Ridge is largely dominated by the retroflection modes of the SEMC (unpublished data).

When the retroflection is in a canonical mode, dipoles similar to that surveyed during the MAD-Ridge cruise are expelled from the SEMC. Surface relative vorticity showed that the dipole surveyed during the MAD-Ridge cruise resulted from the coupling between a large patch of cyclonic vorticity that was formed on the southeastern tip of Madagascar, forcing the SEMC to flow south. This cyclonic patch later detached from the current after forming a dipole with an anticyclonic vorticity patch of the SEMC (Fig. 4).

5.3.2 Influence of sub-mesoscale dynamics:

Our results have shown that sub-mesoscale dynamics may superimpose the dominant mesoscale eddy-driven flow. Some fine-scale undulations of the isopycnals were also evident on the eastern side of the seamount along the west-east transect (X3 in Fig 7). Although there

693 is evidence that they were induced by eddy-topography interactions, they could also be the
694 signature of: i) sub-mesoscale features generated in the frontal region between the two eddies;
695 ii) internal tidal/Lee waves radiating away from the seamount after being generated by
696 tidal/geostrophic flow impinging over the seamount (Nikurashin and Ferrari, 2010). There is
697 evidence too that the northern Madagascar Ridge could be an area of intense internal tide
698 generation (Arbic et al., 2010; A. Koch-Larouy, pers. comm.) and that the steepness of the
699 MAD-Ridge seamount could make it a candidate for internal tide dissipation (Hosegood et al.,
700 2019). Nonetheless, no direct influence of the seamount on the vertical distribution of chl-*a*
701 was observed along the two transects (Fig. 6 and 7). The DCM was even found slightly
702 deeper over the summit (-150 m at station 8) than on the slopes of the seamount. Even if these
703 undulations corresponded to internal waves, the resolution of the CTD vertical profiles along
704 the two transects was too coarse to capture the patchiness of vertical mixing events which by
705 essence act at very local and small scales. The search for local overturning cells through the
706 determination of the Thorpe scale in the CTD vertical profiles (Dillon, 1982; Finnigan et al.,
707 2002) might have provided evidence of vertical mixing, but was beyond the scope of this
708 work.
709
710 *5.3.3 The ghost Taylor column effect*
711 The presence of Taylor columns above seamounts seems to be a deeply anchored
712 theoretical concept for biologists looking for an impact of the seamount on the distribution of
713 the lower trophic components of pelagic ecosystems. Taylor columns may indeed be
714 generated on top of a seamount by mesoscale eddies. However, one still queries their
715 effectiveness in impacting primary production and facilitating retention of organisms in the
716 context of a rapidly changing environment.
717 The time-scale of this biological response vs. the time-scale of ocean circulation variability
718 is an essential aspect of the problem. Although it is generally admitted that phytoplankton
719 responds within a day or two to the presence of nutrients within the euphotic layer, the
720 response of zooplankton is delayed by several weeks (Genin and Boehlert, 1985; Genin and
721 Dower, 2007). The 1993-2016 time-series of surface geostrophic velocity computed from
722 altimetry at the MAD-Ridge seamount was used to estimate the probability of Taylor column
723 occurrences using velocities <30 cm s^{-1} as a proxy (see Appendix). Results show that this
724 threshold was met only 27% of the time over the period 1993-2016 (not shown). In addition,
725 the time-scale (~10 days) of eddy variability in the region (de Ruijter et al., 2004; Nauw et al.,
726 2008; Halo et al., 2014; Ramanantsoa et al., 2020) seems too short to trigger a biological

response of the zooplankton at the seamount (Annasawmy et al., 2020; Noyon et al., 2020). Only 17 incidences of low velocity events lasted >25 days within the 23-year time-series.

6 Summary and conclusions

The dipole surveyed during the MAD-Ridge cruise originated from the SEMC when the latter was in a canonical retroflection mode. In such a mode, intense long-life coherent dipoles are expelled from the SEMC. The cruise highlighted the fact that these dipoles interacted strongly with the complex bathymetry of the northern Madagascar Ridge. By blocking eddy propagation and favouring its erosion, the topography contributes to the stirring of the surrounding water masses by the strong eddy-induced velocities, which themselves contribute indirectly to the mixing of water masses in the region and their subsequent westward advection by non-linear isolated eddies. As such eddies will continue their journey towards the Agulhas Current (Siedler et al., 2009), the northern Madagascar Ridge is concluded to play a key role in World Ocean circulation. In particular, because fresh, cool upwelled water is usually found at the southeastern tip of Madagascar when the SEMC overshoots southwards (Dilmahamod et al., 2019; Ramanantsoa et al., 2020), more of this water mass is expected to be exported within the Agulhas Current (Beal et al., 2006, 2011).

The mesoscale variability in the region is largely constrained by the variability of the SEMC (Ramanantsoa et al., 2020). Eddies are therefore expected to encounter the northern Madagascar Ridge when the SEMC is in the canonical retroflection mode (34% of the time) or early retroflection mode (13% of the time). When the SEMC continues westwards (no retroflection, 53% of the time), the northern Madagascar Ridge sits between the SEMC and the SICC, with limited mesoscale eddies. Current-topography interactions may only then determine the circulation and hydrography of the region.

We stress that a biological signature resulting from a Taylor column effect is unlikely at the MAD-Ridge seamount because of the intense mesoscale variability there. These results are consistent with observations reported by Read and Pollard (2017), who described the circulation and hydrography around six seamounts located over the South West Indian Ridge, in the vicinity of the Agulhas Return Current, an area also characterized by the frequent passage of strong mesoscale eddies.

Further, using satellite-derived chl-*a*, Demarcq et al. (2020) could not identify any phytoplankton signature over the MAD-Ridge seamount. Those authors showed that chl-*a* variability in the region was dominated by filaments torn off from the coastal upwelling cells and advected in the vicinity of the seamount by the mesoscale and sub-mesoscale dynamics.

Therefore, in the vicinity of seamounts where the circulation is dominated by large mesoscale variability, the distribution of chl-*a* is expected to be governed by the mesoscale eddy flow.

Acknowledgements

We thank C. Bachelier and P. Rousselot (IRD, Brest) for their S-ADCP (CB) and CTD and L-ADCP (PR) calibration, and F. Baurand and S. Hillion (IRD, Brest) for the chemical analysis (nutrients and phytoplankton pigments), and the officers, crew and scientists of the RV *Antea* for assistance during the cruise. The work was supported financially and logistically by the Institut de Recherche pour le Développement (IRD) and the Flotte Océanographique Française. Additional funding was received from the Fonds Français pour l'Environnement Mondial (FFEM) on the Areas Beyond National Jurisdiction (ABNJ) in the SWIO and LABEX Mer. The research was carried out under the auspices of the Western Indian Ocean Upwelling Research Initiative (WIOURI), part of the 2016–2020 International Indian Ocean Expedition (IIOE-2) programme.

Appendix

A Taylor cap at the MAD-Ridge seamount

When a geophysical flow encounters a seamount, a closed isolated anticyclonic circulation can grow and remain trapped above the seamount summit. This feature is commonly referred as a Taylor cap or a Taylor column (Huppert, 1975; Huppert and Bryan, 1976). In a situation of moderate stratification, like that found over the northern Madagascar ridge during leg 1, the conditions for a Taylor cap to grow resume to $H_T/(H\ R_o) > 2$ and $R_o < 0.15$, where H_T is the height of the seamount, H the bottom depth, $R_o=U/(f\ L)$ the Rossby number, U the flow velocity, f the Coriolis parameter, L the seamount radius (White et al., 2007; Chapman and Haidvogel, 1992; Sutyrin et al., 2011). Considering the characteristics of the MAD-Ridge seamount (L = 27.5 km and H_T = 1400 m, H = 1600 m) and its latitude (27°30'S), one finds that the most constraining condition relates to the smallness of the Rossby number, so requiring the velocity of the flow to be <30 cm s^{-1}.

References

Alvheim, O., Torstensen, E., Fennessy, S., MacKay, F., Zaera, D., Bemiasa, J., 2009. Cruise reports "Dr Fridtjof Nansen", West Madagascar: Pelagic Ecosystem Survey.

Annasawmy, P., Ternon, J-F., Lebourges-Dhaussy, A., Roudaut, G., Cotel, P., Herbette, S., Ménard, F., Marsac, F., 2020a. Micronekton distribution as influenced by mesoscale

795 eddies, Madagascar shelf and shallow seamounts in the south-western Indian Ocean: an
796 acoustic approach. Deep Sea Res. II (this issue).
797 Arbic, B. K., Wallcraft, A.J., Metzger, E.J., 2010. Concurrent simulation of the eddying
798 general circulation and tides in a global ocean model, Ocean Modell. 32, 175–187.
799 Beal, L.M., Chereskin, T.K., Lenn, Y.D., Elipot, S., 2006. The sources and mixing
800 characteristics of the Agulhas Current. J. Phys. Oceanogr. 36, 2060–2074.
801 Beal, L. M., De Ruijter, W. P. M., Biastoch, A., Zahn, R., 2011. On the role of the Agulhas
802 system in ocean circulation and climate. Nature, 472(7344), 429–436.
803 doi:10.1038/nature09983
804 Boehlert, G.W., Mundy, B.C., 1993. Ichthyoplankton assemblages at seamounts and oceanic
805 islands. Bull. Mar. Sci. 53, 336-361.
806 Capet, X., McWilliams, J.C., Molemaker, M.J., Shchepetkin, A.F., 2008. Mesoscale to
807 submesoscale transition in the California current system. II. Frontal processes. J. Phys.
808 Oceanogr. 38, 44–64.
809 Chapman, D.D., Haidvogel, D.B., 1992. Formation of Taylor caps over a tall isolated
810 seamount in a stratified ocean. Geophys. Astrophys. Fluid Dyn. 64, 31–65.
811 Chelton, D. B., deSzoeke, R.A., Schlax, M.G., El Naggar, K., Siwertz, N., 1998.
812 Geographical variability of the first baroclinic Rossby radius of deformation. J. Phys.
813 Oceanogr. 28, 433–460.
814 Chelton, D.B., Schlax, M.G., Samelson, R.M., de Szoeke, R.A., 2007. Global observations of
815 large oceanic eddies. Geophys. Res. Lett. 34(15). doi.org/10.1029/2007GL030812
816 Clark, M.R., 2001. Are deepwater fisheries sustainable? The example of orange roughy
817 (*Hoplostethus atlanticus*) in New Zealand. Fish. Res. 51, 123–135.
818 Clark, M.R., Rowden, A.A., Schlacher, T., Williams, A., Consalvey, M., Stocks, K.I., Rogers,
819 A.D., O'Hara, T.D., White, M., Shank, T.M., Hall-Spencer, J.M., 2010. The ecology of
820 seamounts: structure, function and human impacts. A. Rev. Mar. Sci. 2, 253–278.
821 Comeau, L.A., Vézina, A.F., Bourgeois, M., Juniper, S.K., 1995. Relationship between
822 phytoplankton production and the physical structure of the water column near Cobb
823 Seamount, northeast Pacific. Deep-Sea Res. I. 42, 993–1005.
824 Demarcq, H., Noyon, M., Roberts, M.J., 2020. Satellite observations of phytoplankton
825 enrichments around seamounts in the South West Indian Ocean, with a special focus on
826 the Walters Shoal. Deep-Sea Res. II (this issue).
827 De Ruijter, W.P.M., van Aken, H.M., Beier, E.J., Lutjeharms, J.R.E., Matano, R.P., Schouten,
828 M.W., 2004. Eddies and dipoles around South Madagascar: formation, pathways and
829 large-scale impact. Deep-Sea Res. I. 51, 383–400.
830 Dilmahamod, A.F., Penven, P., Aguiar-González, B., Reason, C.J.C., Hermes, J.C., 2019. A
831 new definition of the South-East Madagascar bloom and analysis of its variability. J.
832 Geophys. Res. Oceans,124. doi.org/10.1029/2018JC014582.
833 Dillon, T.M., 1982. Vertical overturns: a comparison of Thorpe and Ozmidov lengthscales. J.
834 Geophys. Res., 87, 9601–9613.
835 Di Marco, S.F., Chapman, P., Nowlin, W.D., Hacker, P., Donohue, K., Luther, M., Johnson,
836 G.C., Toole, J., 2002. Volume transport and property distributions of the Mozambique
837 Channel. Deep-Sea Res. II. 49, 1481–1511.
838 Dower, J., Freeland, H., Juniper, K., 1992. A strong biological response to oceanic flow past
839 Cobb Seamount. Deep-Sea Res. I. 39, 1139–1145.
840 Dower, J., Mackas, D. L., 1996. "Seamount effects" in the zooplankton community near Cobb
841 Seamount. Deep Sea Res. I. 43, 837–858.
842 Emery, W.J., Meincke, J., 1986. Global water masses: summary and review. Oceanologica
843 Acta 9(4).

Egbert, G.D., Erofeeva, S.Y., 2002. Efficient inverse modelling of barotropic ocean tides. J. Atmos. Oceanic Technol. 19, 183–204.
Finnigan, T., Luther, D., Lukas, R., 2002. Observations of enhanced diapycnal mixing near the Hawaiian Ridge. J. Phys. Oceanogr. 32, 2988–3002.
Garcia, H.E., Weathers, K., Paver, C.R., Smolyar, I., Boyer, T.P., Locarnini, R.A., Zweng, M.M., Mishonov, A.V., Baranova, O.K., Seidov, D., Reagan, J.R., 2018. World Ocean Atlas 2018, Volume 3: Dissolved Oxygen, Apparent Oxygen Utilization, and Oxygen Saturation. A. Mishonov (Technical Ed.); NOAA Atlas NESDIS 83, 38 pp.
Garrett, C., 2003. Internal tides and ocean mixing. Science 301, 1858–1859.
Genin, A., 2004. Bio-physical coupling in the formation of zooplankton and fish aggregations over abrupt topographies. J. Mar. Syst. 50, 3–20.
Genin, A., Boehlert, G.W., 1985. Dynamics of temperature and chlorophyll structures above a seamount: an oceanic experiment. J. Mar. Res. 43, 907–924.
Genin, A., Dower, J.F., 2007. Seamount plankton dynamics. In Seamounts: Ecology, Fisheries and Conservation. Pitcher T.J., Morato, T., Hart, P.J.B., Clark, M.R., Haggan, N., Santos., R.S., (Eds) Blackwell Publishing, Oxford, UK. 84–100.
Halo, I., Penven, P., Backeberg, B., Ansorge, I., Shillington, F., Roman, R., 2014. Mesoscale eddy variability in the southern extension of the East Madagascar Current: seasonal cycle, energy conversion terms, and eddy mean properties. J. Geophys. Res. 119, 7324–7356.
Hanawa, K., Talley, L.D., 2001. Mode waters. In Ocean Circulation and Climate: Observing and Modelling the Global Ocean. Siedler, G., Church, J., Gould, J. (Eds). Elsevier, New York. 373–392.
Herbette, S., Morel, Y., Arhan, M., 2003. Erosion of a surface vortex by a seamount. J. Phys. Oceanogr. 33, 1664–1679.
Herbette, S. 2003. Erosion des tourbillons océaniques : influence de la topographie et d'un front isopycnal – application aux anneaux des aiguilles. PhD thesis, University of Brest.
Herbette, S., Morel, Y., Arhan, M., 2005. Erosion of a surface vortex by a seamount on the beta plane, J. Phys. Oceanogr. 35, 2012–2030.
Hogg, N.G., Stommel, H.M., 1985. The heton, an elementary interaction between discrete baroclinic geostrophic vortices, and its implication concerning eddy heat-flow. Proc. R. Soc. Lond. 397, 1–20. doi.org/10.1098/rspa.1985.0001.
Hosegood, P.J. Nimmo-Smith, W.A.M., Proud, R., Adams, K., Brierley, A.S., 2019. Internal lee waves and baroclinic bores over a tropical seamount shark 'hot-spot', Prog. Oceanogr. 172, 34–50. doi.org/10.1016/j.dsr2.2020.104744.
Huppert, H., 1975. Some remarks on the initiation of inertial Taylor columns. J. Fluid Mech. 67, 397–412.
Huppert, H., Bryan, K., 1976. Topographically generated eddies. Deep-Sea Res. 23, 655–679.
Kermabon, C., Le Bot, P., Thierry, V., Lherminier, P., Branellec, P., 2015. CADYHAC: Chaîne d'Ajustage des Données d'HYdrologie Après Campagne – Documentation utilisateur (V1.1). R.INT. ODE/LPO/15-01.
Kitchingman, A., Lai, S., Morato, T., Pauly, D., 2007. How many seamounts are there and where are they located. In Pitcher, T.J., Morato, T., Hart, P.J.B., Clark, M.R., Haggan, N., Santos, R.S. (Eds). Seamounts: Ecology, Fisheries and Conservation. Blackwell Publishing, Oxford, UK. 26–40.
Koslow, J.A., 1997. Seamounts and the ecology of deep-sea fisheries. Am. Scient. 85, 168–176.
Lavelle, J.W., Mohn, C., 2010. Motion, commotion, and biophysical connections at deep ocean seamounts. Oceanogr. 23, 90–103.

Le Bot, P., Kermabon, C., Lherminier, P., Gaillard, F., 2011. CASCADE V6.1 : Logiciel de validation et de visualisation des mesures ADCP de coque. OPS/LPO 11-01. https://archimer.ifremer.fr/doc/00342/45285/

Legal, C., Klein, P., Treguier, A-M., Paillet, J., 2007. Diagnosis of the vertical motion in a mesoscale stirring region. J. Phys. Oceanogr. 37, 1413–1424, doi: 10.1175/JPO3053.1

Lévy, M., 2008. The modulation of biological production by oceanic mesoscale turbulence. Lect. Notes Physics 744, 219–261.

Locarnini, R.A., Mishonov, A.V., Antonov, J.I., Boyer, T.P., Garcia, H.E., Baranova, O.K., Zweng, M.M., Paver, C.R., Reagan, R., Johnson, D.R., Hamilton, M., Seidov, D., 2013. World Ocean Atlas 2013. Vol. 1: Temperature., S. Levitus, 3028 Ed.; A. Mishonov, Technical Ed.; NOAA Atlas NESDIS, 73 (September), 40, doi:10.3029 1182/blood-2011-06-357442.

Lutjeharms, J., Machu, E., 2000. An upwelling cell inshore of the East Madagascar Current. Deep-Sea Res. I. 47, 2405–2411. http://dx.doi.org/ 10.1016/S0967-0637(00)00026-1.

Marsac, F., Galletti, F., Ternon, J-F., Romanov, E.V., Demarcq, H., Corbari, L., Bouchet, P., Roest, W.R., Jorry, S.J., Olu, K., Loncke, L., Roberts, M.J., Ménard, F., 2020. Seamounts, plateaus and governance issues in the southwestern Indian Ocean, with emphasis on fisheries management and marine conservation, using the Walters Shoal as a case study for implementing a protection framework. Deep-Sea Res. II (this issue).

Mason, E., Colas, F., Molemaker, J., Shchepetkin, F., Troupin, C., McWilliams, J.C., Sangra, P., 2011. Seasonal variability of the Canary Current: a numerical study. J. Geophys. Res. 116, doi:10.1029/2010/JC006665.

McGillicuddy, D.J., Robinson, A.R., Siegel, D.A., Jannasch, H.F., Johnson, R., Dickey, T. D., McNeil, J., Michaels, A.F., Knap, A.H., 1998. Influence of mesoscale eddies on new production in the Sargasso Sea. Nature 394, 263–266.

McWilliams, J.C., 2016. Submesoscale currents in the ocean. Proc. R. Soc. A 472: 20160117. http://dx.doi.org/10.1098/rspa.2016.0117

McWilliams, J., Flierl, G., 1979. On the evolution of isolated nonlinear vortices. J. Phys. Oeanogr. 9, 1155–1181.

Morel, Y., 1995. The influence of an upper thermocline current on intrathermocline eddies. J. Phys. Oeanogr. 25, 3247–3252.

Morel, Y., McWilliams, J.C., 1997. Evolution of isolated interior vortices in the ocean., J. Phys. Oeanogr., 27,727–748.

Mouriño, B., Fernández, E., Serret, P., Harbour, D., Sinha, B., Pingree, R., 2001. Variability and seasonality of physical and biological fields at the Great Meteor Tablemount (subtropical NE Atlantic). Oceanologica Acta 24, 167–185.

Mullineaux, L.S., Mills, S., 1997. A test of the larval retention hypothesis in seamount-generated flows. Deep-Sea Res. 44, 745–770.

Nauw, J.J., van Aken, H.M., Lutjeharms, J.R.E., de Ruijter, W.P.M., 2006. Intrathermocline eddies in the southern Indian Ocean. J. Geophys. Res. 111(C3). doi.org/10.1029/2005JC002917

Nauw, J.J., van Aken, H.M., Webb, A., Lutjeharms, J.R.E., de Ruijter, W.P.M., 2008. Observations of the southern East Madagascar Current and undercurrent and countercurrent system. J. Geophys. Res. 113(C8). doi.org/10.1029/2007JC004639

New, A.L., Alderson, S.G., Smeed, D.A., Stansfield, K.L., 2007. On the circulation of water masses across the Mascarene Plateau in the South Indian Ocean. Deep-Sea Res. I. 54, 42–74.

New, A.L., Stansfield, K., Smythe-Wright, D., Smeed, D.A., Evans, A.J., Alderson, S.G., 2005. Physical and biochemical aspects of the flow across the Mascarene Plateau in the Indian Ocean. Phil. Trans. R. Soc. Lond. A. 363, 151–168.

Nikurashin, M., Ferrari, R., 2010. Radiation and dissipation of internal waves generated by geostrophic motions impinging on small-scale topography: theory. J. Phys. Oceanogr. 40, 1055–1074. doi: 10.1175/2009JPO4199.1

Noyon, M., Rasoloarijao, Z., Huggett, J., Ternon, J-F., Roberts, M., 2020. Comparison of mesozooplankton communities at three shallow seamounts in the South West Indian Ocean. Deep Sea Res. II (this issue).

O'Connor, B.M., Fine, R.A., Maillet, K.A., Olson D.B., 2002. Formation rates of subtropical-underwater in the Pacific Ocean. Deep-Sea Res. I. 49, 1571–1590.

Okubo, A., 1970. Horizontal dispersion of floatable particles in the vicinity of velocity singularities such as convergences. Deep-Sea Res. 17, 445–454.

Oschlies, A., Garçon, V., 1998. Eddy-induced enhancement of primary production in a model of the North Atlantic Ocean. Nature 394, 266–269.

Oudot, C., Morin, P., Baurand, F., Wafar, M., Le Corre, P., 1998. Northern and southern water masses in the Equatorial Atlantic: distribution of nutrients on the WOCE A6 and A7 lines. Deep-Sea Res. I. 45, 873–902.

Pilo, G.S., Mata, M.M., Azevedo, L.L., 2015. Eddy surface properties and propagation at Southern Hemisphere western boundary current systems. Ocean Sci. 11, 629–641.

Pitcher, T.J., Clark, M.R., Morato, T., Watson, R., 2010. Seamount fisheries: do they have a future? Oceanography 23, 1. 134–144.

Pollard, R.T., Regier, L.A., 1992. Vorticity and vertical circulation at an ocean front. J. Phys. Oceanogr. 22, 609–625.

Pollard, R., Read, J., 2017. Circulation, stratification and seamounts in the Southwest Indian Ocean. Deep-Sea Res. II. 136, 36–43. doi:/10.1016/j.dsr2.2015.02.018

Ponsoni, L., Aguiar-Gonzalez, Ridderinkhof, H., Maas, L.R., 2016. The East Madagascar Current; volume transport and variability based on long-term obervations., J. Phys. Oceanogr. 46, 1045–1065, doi:10.1175/JPO-D-15-0154.1

Pous, S., Lazure, P., André, G., Dumas, F., Halo, I., Penven, P., 2014. Circulation around La Réunion and Mauritius islands in the south-western Indian Ocean: a modeling perspective. J. Geophys. Res. Oceans 119, 1957–1976. doi:10.1002/2013JC009704

Pripp, T., Gammelsrod, T., Krakastad, J., 2014. Physical influence on biological production along the western shelf of Madagascar. Deep-Sea Res. II. 100, 174–183.

Quartly, G.D. (2006) RRS Discovery Cruise 288, 26 January - 21 February 2005. Madagascar Experiment (MadEx). National Oceanography Centre, Southampton, Cruise Report 8. Southampton, UK, National Oceanography Centre Southampton, 105 pp.

Quartly, G.D., Buck, J.J.H., Srokosz, M.A., Coward, A.C., 2006. Eddies around Madagascar – the retroflection re-considered. J. Mar. Syst. 63, 115–129.

Ramanantsoa, J.D., Krug, M., Penven, P., Rouault, M., Gula, J., 2018. Coastal upwelling south of Madagascar: temporal and spatial variability. J. Mar. Syst. 178, 29–37.

Ramanantsoa, J.D., P. Penven, P., Raj, R.P., Renault, L., Ponsoni, L., Ostrowski, M., Dilahamod, A.F., Rouault, M., 2020. Where and how the East Madagascar Current retroflection generates? (submitted to J. Geophys. Res.)

Read, J., Pollard, R.T., 2017. An introduction to the physical oceanography of six seamounts in the southwest Indian Ocean. Deep-Sea Res. II. 136, 44–58. doi:/10.1016/j.dsr2.2015.06.022

Richardson, P.L., Tychensky, A., 1998. Meddy trajectories in the Canary Basin measured during the SEMAPHORE experiment, 1993–1995. J. Geophys. Res. 103(C11), 25029–25045.

Ridderinkhof, W., Le Bars, D., von der Heydt, A.S., De Ruijter, W.P.M., 2013. Dipoles of the South East Madagascar Current. Geophys. Res. Lett. 40(3), 558–562.

Roberts, M.J., Ternon J-F., Marsac, F., Noyon, M., Payne, A.I.L., 2020. The MADRidge Project: Bio-Physical coupling around a shallow seamount on the northern Madagascar Ridge, South West Indian Ocean. Deep-Sea Res. II. (this issue).

Rogers, A. D., 1994. The biology of seamounts. Adv. Mar. Biol. 30, 305–350.

Rogers, A.D., 2016. Pelagic ecology of the South West Indian Ocean Ridge seamounts: introduction and overview. Deep-Sea Res. II. 136, 1–4. doi;/10.1016/j.dsr2.2016.12.009

Rousselet, L., Doglioli, A. M., de Verneil, A., Pietri, A., Della Penna, A., Berline, L., Marrec, P., Grégori, G., Thyssen, M., Carlotti, F., Barrillon, S., Simon-Bot, F., Bonal, M., d'Ovidio, F., Potrenko, A., 2019. Vertical motions and their effects on a biogeochemical tracer in a cyclonic structure finely observed in the Ligurian Sea. J. Geophys. Res. Oceans 124, 3561–3574. https://doi.org/10.1029/2018JC014392.

Rowden, A.A., Dower, J.F., Schlacher, T.A., Consalvey, M., Clark, M.R., 2010. Paradigms in seamount ecology: fact, fiction and future. Mar. Ecol. 31, 226–241. https://doi.org/10.1111/j.1439-0485.2010.00400.x

Royer, T.C.1978. Ocean eddies generated by seamounts in the North Pacific. Science 199, 1063–1064.

Schlacher, T.A., Rowden, A.A., Dower, J.J., Consalvey, M., 2010. Seamount science scales undersea mountains: new research and outlook. Mar. Ecol. 31(Suppl. 1), 1–13.

Siedler, G., Rouault, M., Biastoch, A., Backeberg, B., Reason, C.J.C., Lutjeharms, J.R.E., 2009. Modes of the southern extension of the East Madagascar Current. J. Geophys. Res. 114(C01005). doi:10.1029/2008JC004921

Sinha, M.C., Louden, K.E., Barry Parsons, B., 1981. The crustal structure of the Madagascar Ridge. Geophys. J. R. Astron. Soc. 66, 351–377.

Sprintall, J., Tomczak, M., 1992. On the formation of central water and thermocline ventilation in the southern hemisphere. Deep-Sea Res. I. 40, 827–848.

Sutyrin, G., Herbette, S., Carton, X., 2011. Deformation and splitting of baroclinic eddies encountering a tall seamount. Geophys. Astrophys. Fluid Dyn. 105, 478–505. doi: 10.1080/03091929.2011.566566.

Sutyrin, G., Morel, Y., 1997. Intense vortex motion in a stratified fluid on the beta-plane: an analytical theory and its validation. J. Fluid Mech. 336, 203–220. doi:10.1017/S0022112096004685.

Talley, L.D., Pickard, G.L., Emery, W.J., Swift, J.H., 2011. Descriptive Physical Oceanography, 6th edn. Academic Press, New York.

Thurnherr, A.M., 2014. How to process LADCP data with the LDEO Software (Versions IX.7 – IX.10).

Vandermeirsch, F., Morel, Y., Sutyrin, G., 2001. The net advective effect of a vertically sheared current on a coherent vortex. J. Phys. Oceanogr. 31, 2210–2225. doi: 10.1175/1520-0485(2001)031<2210:TNAEOA>2.0.CO;2.

Vianello, P., Ternon, J-F., Demarcq, H., Herbette, S., Roberts, M.J., 2020. Ocean currents and gradients of surface layer properties in the vicinity of the Madagascar Ridge, South West Indian Ocean. Deep-Sea Res. II (this issue).

Verron, J., Le Provost, C., 1985. A numerical study of quasigeostrophic flow over topography. J. Fluid Mech. 154, 231–252.

Voldsund, A., Aguiar-Gonzalez, B., Grammelsrod, T., Krakstad, J-O., Ullgren, J., 2017. Observations of the East Madagascar Current system: dynamics and volume transports. J. Mar. Res. 75, 531–555.

Weiss, J., 1991. The dynamics of enstrophy transfer in two-dimensional hydrodynamics. Physica D 48, 273–294.

White, M., Bashmachnikov, I., Arístegui, J., Martins, A., 2007. Physical processes and seamount productivity. In Pitcher, T.J., Morato, T., Hart, P.J.B., Clark, M.R., Haggan,

N., Santos, R.S. (Eds), Seamounts: Ecology, Fisheries and Conservation. Blackwell Publishing, Oxford, UK. 65–84.
WOA18. World Ocean Atlas 2018. Temperature: Locarni et al., 2013; Salinity: Zweng et al., 2018; Oxygen: Garcia et al., 2018.
Zweng, M.M., Reagan, J.R., Seidov, D., Boyer, T.P., Locarnini, R.A., Garcia, H.E., Mishonov, A.V., Baranova, O.K., Weathers, K., Paver, C.R., Smolyar, I., 2018. World Ocean Atlas 2018, Volume 2: Salinity. A. Mishonov (Technical Ed.). NOAA Atlas NESDIS 82, 50 pp.

Figure Legends

Fig. 1. Mean (1995–2015) surface eddy kinetic energy (EKE) of the western Indian Ocean with contours (1000 and 3000 m) of the satellite (SRTM) bathymetry superimposed (solid grey). The black box indicates the area in which mesoscale eddies was tracked. The three seamounts surveyed during the broader MADRidge project are represented: Walters Shoal, south of Madagascar, La Pérouse, north of Réunion Island (yellow circles), MAD-Ridge seamount, northern Madagascar Ridge (red circle). Black arrows schematize the major features of the oceanic circulation in the region: Agulhas Current (AC); Mozambique Channel Anticyclonic Eddies (MCAE); South Equatorial Current (SEC); North East Madagascar Current (NEMC); South East Madagascar Current (SEMC); South Indian Counter Current (SICC).

Fig. 2. (a) Satellite (SRTM) bathymetry with the location of the east–west and south–north transects surveyed during the MAD-Ridge Leg 1 cruise. The two transects intersect at the MAD-Ridge seamount. Positions of the CTD and fluorometer vertical profiles (stations) are superimposed (black dots). An index is given to each cast (yellow boxes). (b) Same as (a), zooming in over the seamount summit. The SRTM bathymetry has been replaced by one resulting from optimal interpolation of echo-sounder bathymetry data collected on board the RV *Antea* during the cruise. Casts 8, 21 and 22 are located over the summit (depth ~240 m), whereas casts 7, 9, 20 and 23 are located over the slopes of the seamount (depth ~650 m).

Fig. 3. (Top) Weekly average sea level anomaly (SLA) describing the mesoscale eddy field in place during the MAD-Ridge Leg 1 cruise, with geostrophic currents (vectors) calculated from satellite ADT superimposed: (top left) 16 November 2016; (top right) 20 November 2016. The location of the two transects (black solid lines) is superimposed on the altimetry maps. The trajectory of the cyclone and anticyclone forming a mesoscale eddy dipole (thin black lines with dots) is superimposed from 29 October to 24 December 2016, with positions of the eddy centres reported every 7 days (dots). (Bottom) Low-pass filtered S-ADCP surface current along the west–east (bottom left) and south–north (bottom right) transects. The west–east and south–north transects were undertaken between 14 and 18 November and 19 and 23 November 2016, respectively.

Fig. 4. Maps (from 16 October to 14 December 2016) of surface geostrophic relative vorticity (s^{-1}) over the northern Madagascar Ridge calculated from weekly satellite absolute dynamic topography (ADT). The ±20 cm SLA contours delimiting the cores of the anticyclonic and cyclonic eddies forming the mesoscale eddy dipole are superimposed (solid white).

Fig. 5. Vertical sections of S-ADCP data along the west–east (14-18 November, left) and south–north (19-23 November, right) transects, with iso-density (kg m^{-3}) contours superimposed (solid black). Vertical sections include the current magnitude (a, b), and its

zonal u-component (c, d) and meridional v-component (e, f). Iso-contours of current magnitude (solid white) are superimposed every 50 cm s^{-1} from −1 m s^{-1} to 1 m s^{-1}. Indices of the CTD-fluorometer profiles (stations) are reported on the top x-axis and superimposed as black dashed vertical lines. The seamount is also superimposed (black filled).

Fig. 6. Vertical sections of geostrophic (a, b) and ageostrophic (c, d) current components along the west-east (14–18 November) (left) and south–north (19–23 November) (right) transects, with iso-density (kg m^{-3}) contours superimposed (solid black). The meridional v-component/zonal u-component is shown for the east–west and south–north transects.

Fig. 7. Vertical sections of conservative temperature (°C), absolute salinity (g kg^{-1}), dissolved oxygen (µmol kg^{-1}), potential vorticity (x10-11 s^{-1}) and chl-*a* (mg m^{-3}), along the west–east transect (stations 1–15), with iso-density (kg m^{-3}) contours superimposed (solid black). The blue triangle at 46.25°E refers to the seamount. Vertical dashed lines indicate the position of the CTD vertical profiles. Station indices are reported on the top x-axis. Note the reduced vertical scale (0–500 m) used for potential vorticity and chl-*a*. Important features described in the text are reported: X1: anticyclone (STUW + high salinity + high O_2); X2: cyclone (STUW + high chl-*a*); X3: vertical deviations of the isopycnals; X4: oxygen hotspot within the SICW.

Fig. 8. Same as Fig. 7, for the north–south transect. X1: Anticyclone (STUW + high salinity + high O_2); X5: subsurface oxygen hotspot; X6: high chl-*a* (Madagascar Shelf-enriched waters); X7: vertical undulations of isopycnal depth.

Fig. 9. (a, b) CT-SA diagram, with iso-density (kg m^{-3}) contours superimposed (solid black) for all CTD casts of the MAD-Ridge Leg 1 cruise. In (a), the dots' colour indicates whether the CTD cast was within the cyclonic eddy (blue, stations 2–4), the anticyclonic eddy (red, stations 8–13 and 16–26), the frontal region in between the two eddies (green, stations 5–7), or a non-classified region (grey). Station 28 is highlighted in black dots. In (b), the colour scale represents the depth of measurement. Water masses are identified: TSW = Tropical Surface Water, STUW = Subtropical Underwater, SAMW = Sub Antarctic Mode Water, SEISAMW = South East Indian Sub Antarctic Mode Water, AAIW = Antarctic Intermediate Water. (c) Same as (a) for a CT-O_2 diagram.

Fig. 10. 3-day composite (20–22 November 2016) map of satellite chl-*a* with geostrophic current vectors superimposed (black arrows). The positions of the anticyclonic (AC) and cyclonic (C) eddy centres are also superimposed, as well as the two transects surveyed during the MAD-Ridge Leg 1 cruise (solid black and red). The red portion of the south–north transect corresponds to the *in situ* fluorometer profiles that showed high chl-*a* concentrations when integrated vertically.

Fig. 11. Comparative evolution of sea level anomaly (SLA) at the centre of the cyclonic (blue) and anticyclonic (red) eddies, and their respective maximum satellite chl-*a* concentrations (green dotted/solid for the cyclone/anticyclone, respectively) from 25 November to 25 December 2016, including the MAD-Ridge cruise period. The increase of chl-*a* concentration during the growing phase of the cyclone suggests a phytoplankton response to eddy pumping.

Fig. 12. Vertical sections of nitrate concentration (µmol kg^{-1}) along the (a) west–east and (b) south–north transects, with iso-density (kg m^{-3}) contours superimposed (solid black). Dashed vertical lines indicate the position of the CTD vertical profiles and black dots show the sampling depths. Station indices are reported on the top x-axis.

1142
1143

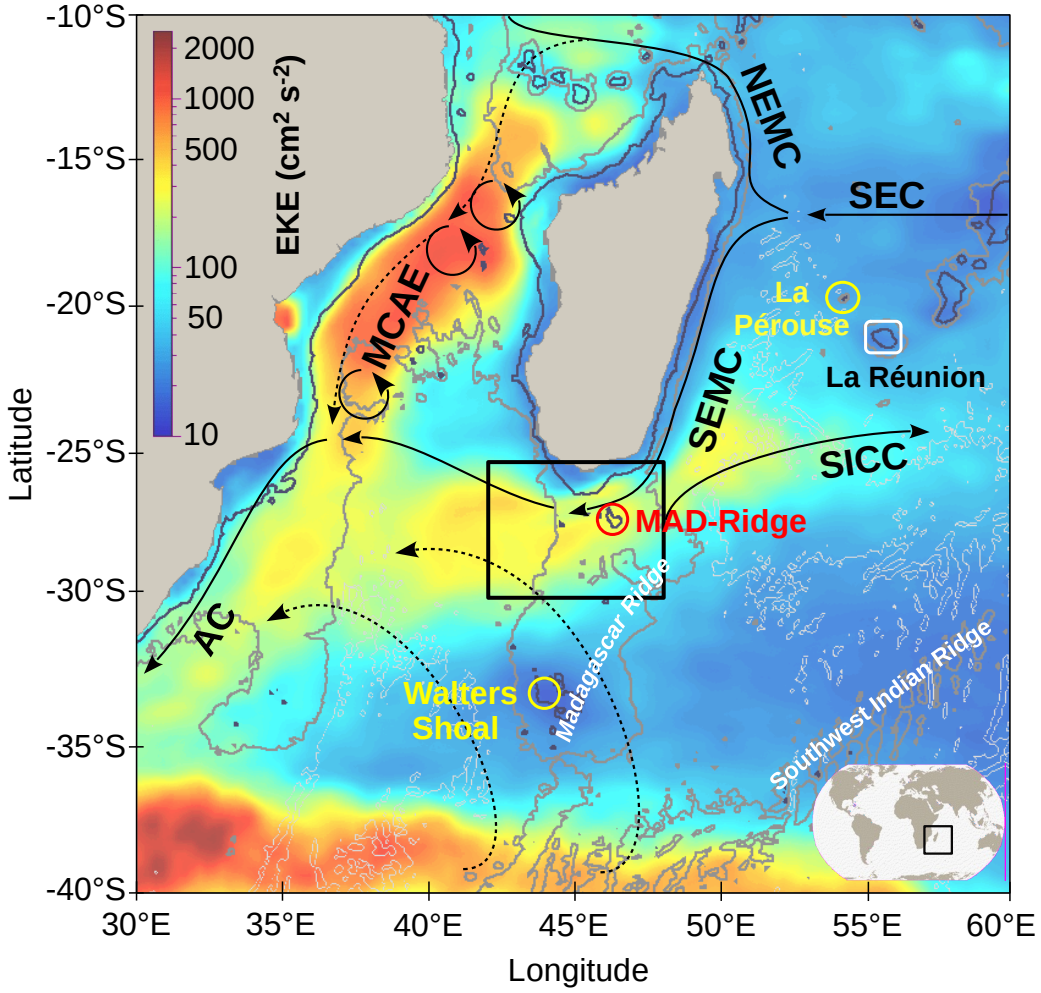
-10°S
-15°S
-20°S
-25°S
-30°S
-35°S
-40°S
Latitude
30°E
35°E
40°E
45°E
50°E
55°E
60°E
Longitude
2000
1000
500
100
50
10
EKE (cm² s⁻²)
NEMC
SEC
MCAE
La Pérouse
La Réunion
SEMC
SICC
MAD-Ridge
AC
Walters Shoal
Madagascar Ridge
Southwest Indian Ridge

Figure 1

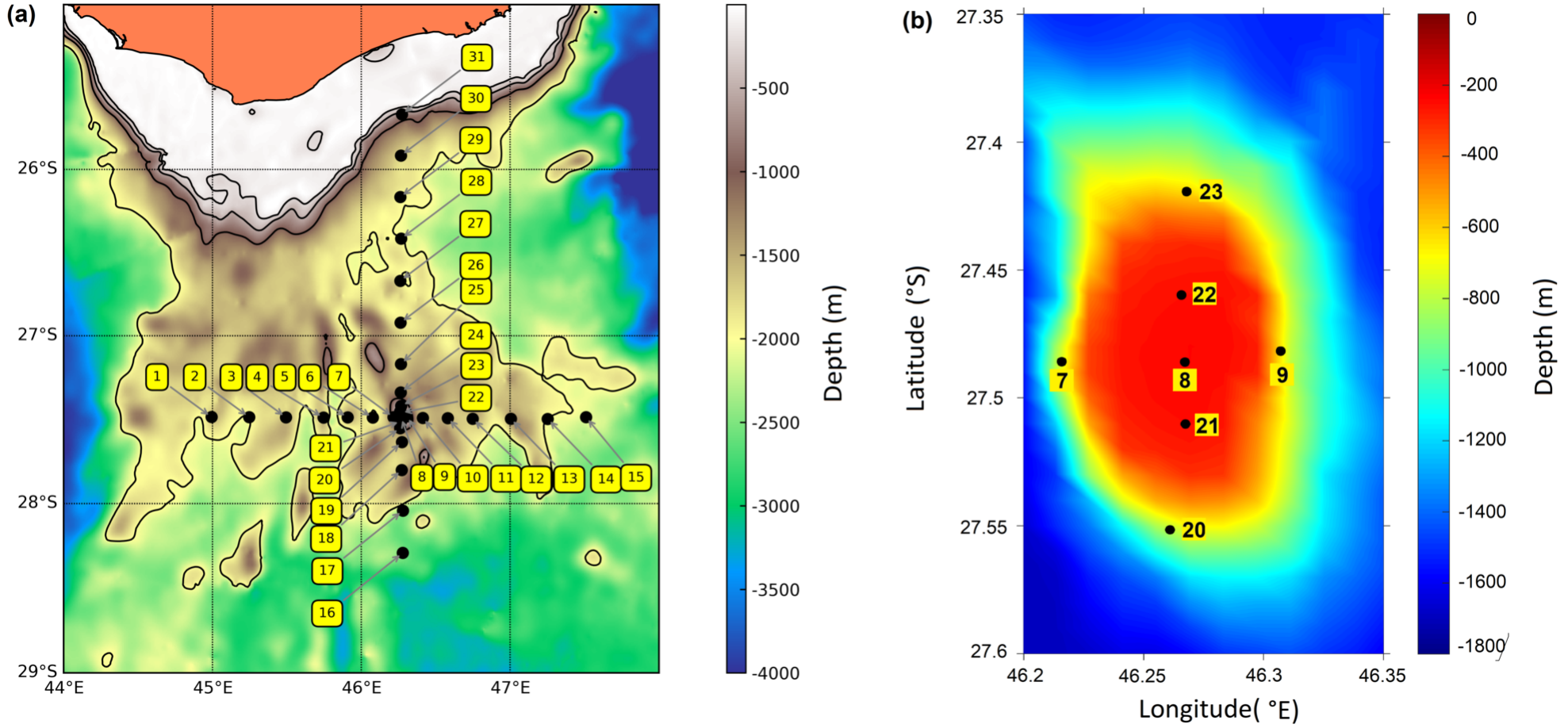
(a)
26°S
27°S
28°S
29°S
44°E
45°E
46°E
47°E
1
2
3
4
5
6
7
8
9
10
11
12
13
14
15
16
17
18
19
20
21
22
23
24
25
26
27
28
29
30
31
-500
-1000
-1500
-2000
-2500
-3000
-3500
-4000
Depth (m)
(b)
27.35
27.4
27.45
27.5
27.55
27.6
Latitude (°S)
46.2
46.25
46.3
46.35
Longitude(°E)
7
8
9
20
21
22
23
0
-200
-400
-600
-800
-1000
-1200
-1400
-1600
-1800
Depth (m)

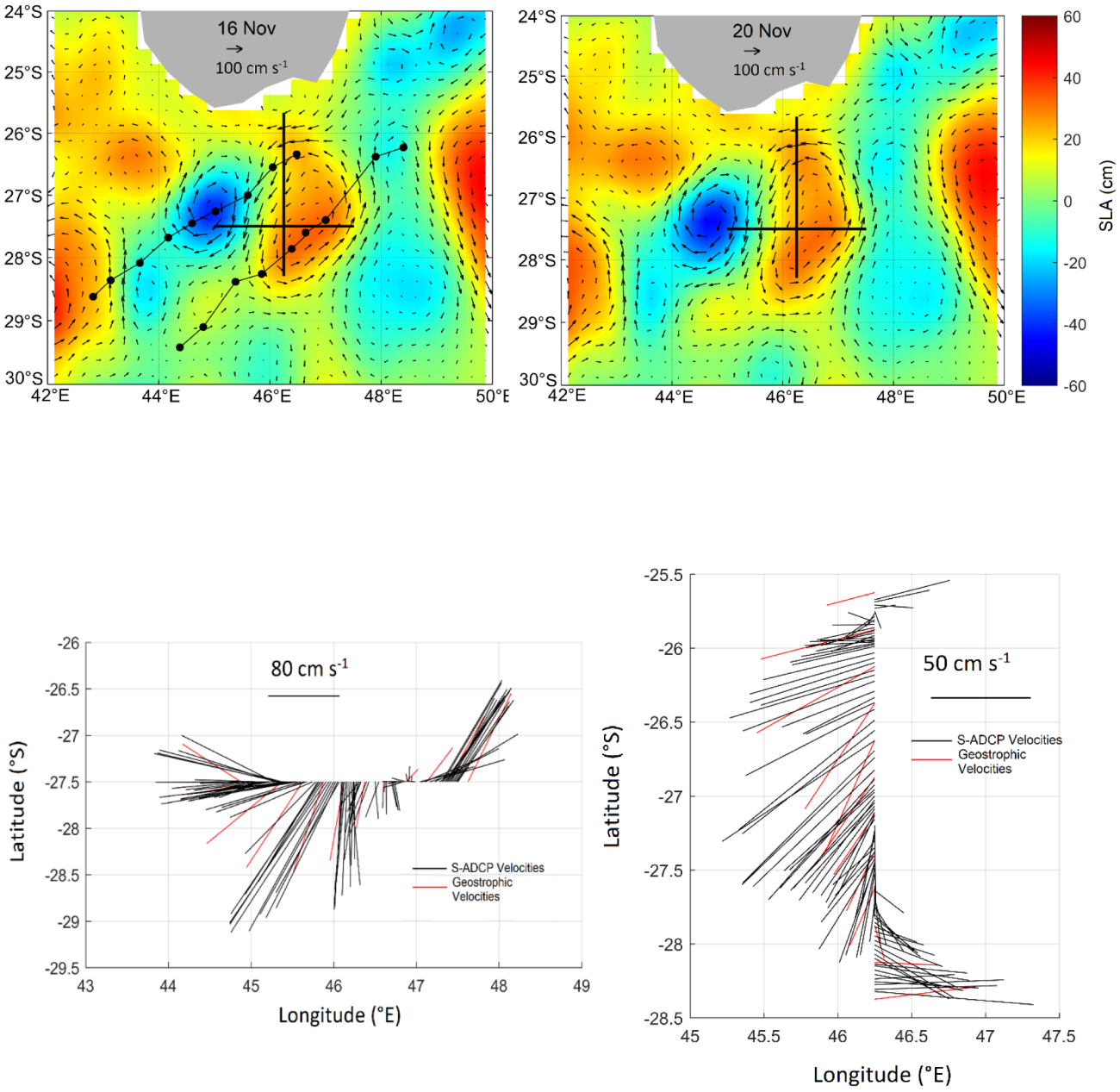
16 Nov
100 cm s-1
20 Nov
100 cm s-1
SLA (cm)
80 cm s-1
S-ADCP Velocities
Geostrophic Velocities
Latitude (°S)
Longitude (°E)
50 cm s-1
S-ADCP Velocities
Geostrophic Velocities
Latitude (°S)
Longitude (°E)

Figure 3

16 Oct
26 Oct
2 Nov
9 Nov
16 Nov
23 Nov
30 Nov
7 Dec
14 Dec
24°S
25°S
26°S
27°S
28°S
29°S
30°S
42°E
44°E
46°E
48°E
50°E
-20
20
5
4
3
2
1
0
-1
-2
-3
-4
-5
Relative Vorticity (s^{-1})

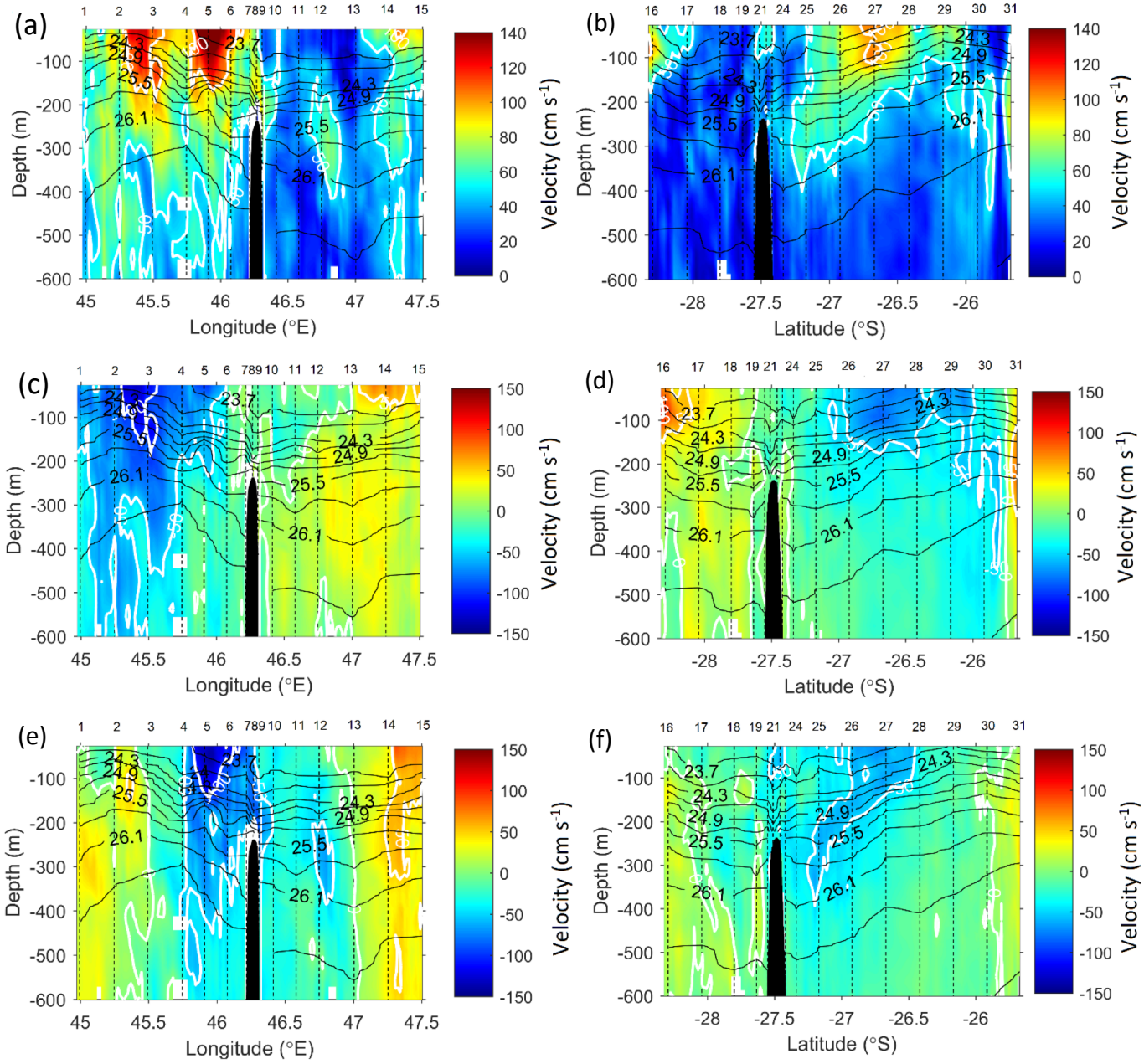
(a)
(b)
(c)
(d)
(e)
(f)
Depth (m)
Longitude (°E)
Latitude (°S)
Velocity (cm s-1)
23.7
24.3
24.9
25.5
26.1

Fig. 5

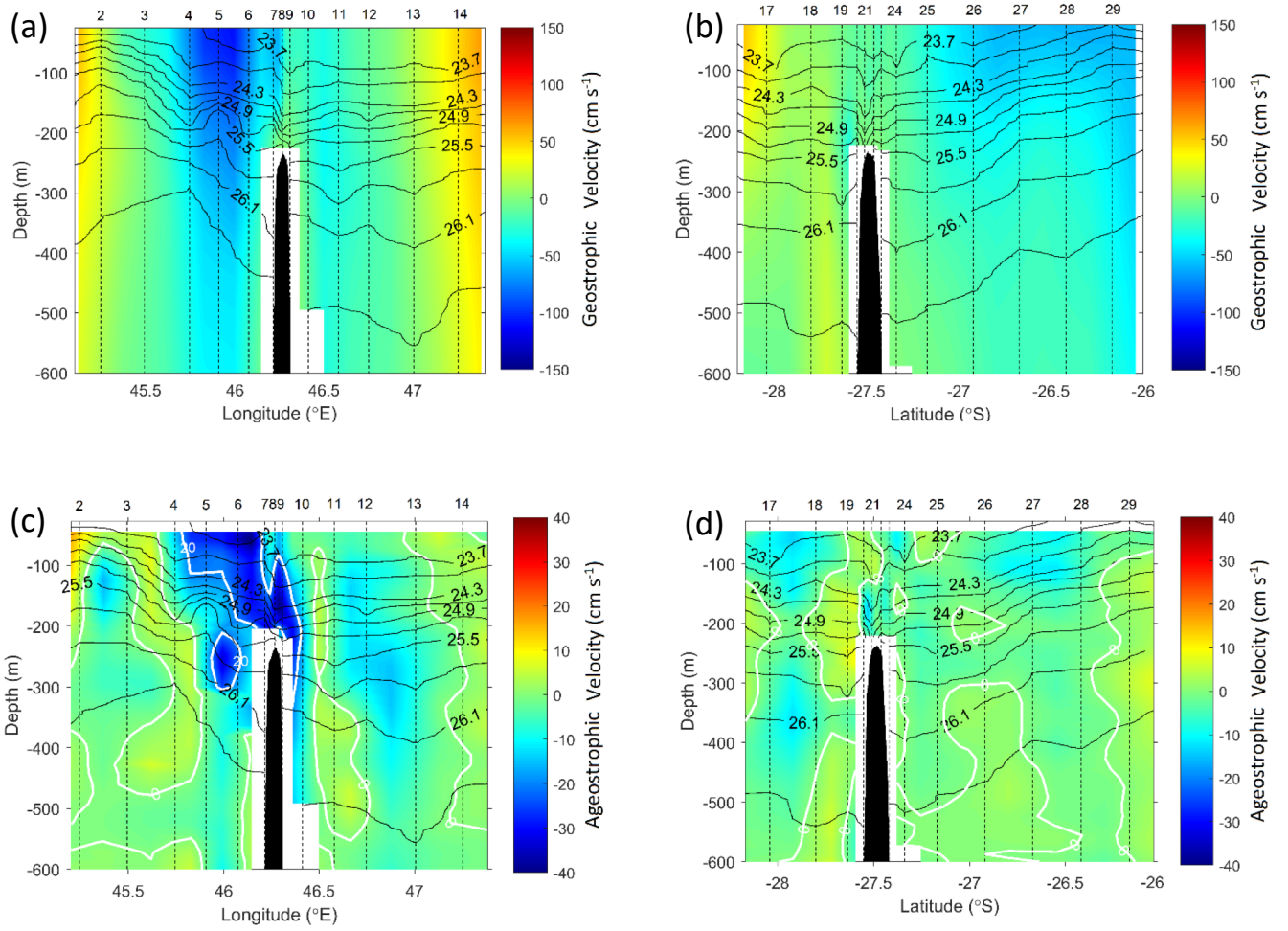
(a)
(b)
(c)
(d)
Depth (m)
Longitude (°E)
Latitude (°S)
Geostrophic Velocity (cm s-1)
Ageostrophic Velocity (cm s-1)
23.7
24.3
24.9
25.5
26.1

Fig. 6:

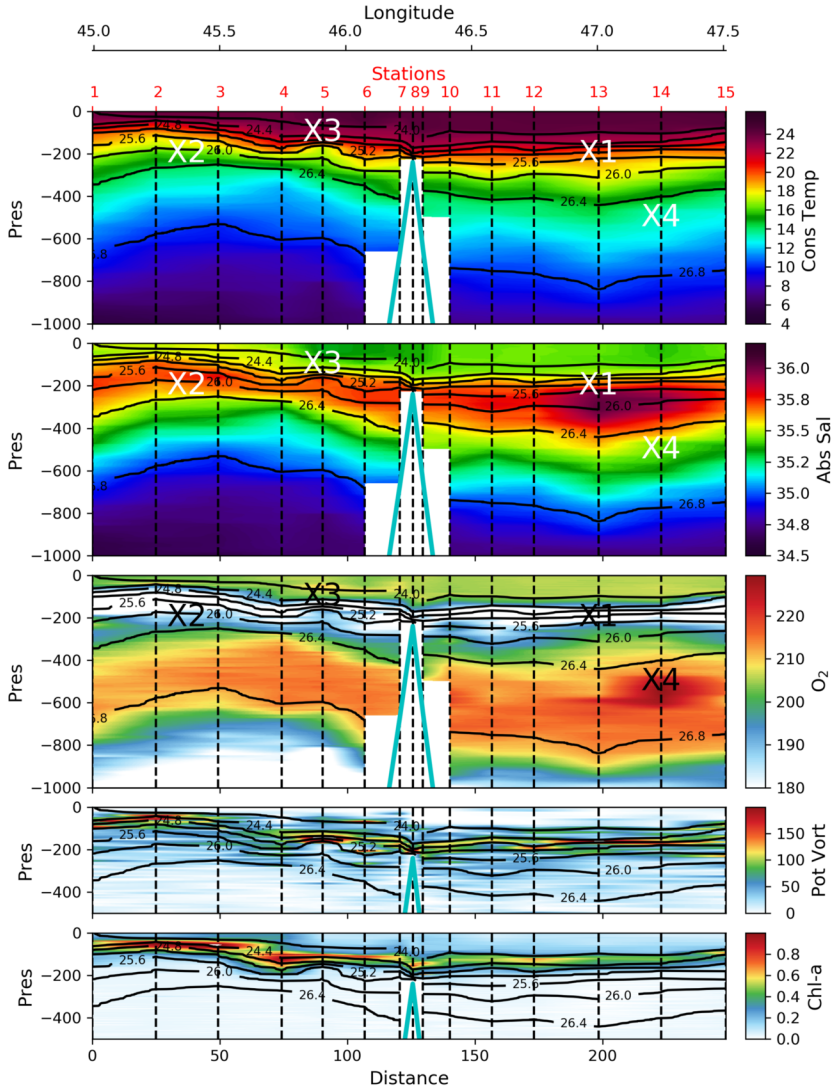
Longitude
45.0
45.5
46.0
46.5
47.0
47.5
Stations
1
2
3
4
5
6
7
8
9
10
11
12
13
14
15
Pres
0
−200
−400
−600
−800
−1000
X1
X2
X3
X4
24.8
24.4
24.0
25.6
25.2
26.0
26.4
26.8
Cons Temp
24
22
20
18
16
14
12
10
8
6
4
Abs Sal
36.0
35.8
35.5
35.2
35.0
34.8
34.5
O2
220
210
200
190
180
Pot Vort
150
100
50
0
Chl-a
0.8
0.6
0.4
0.2
0.0
0
50
100
150
200
Distance

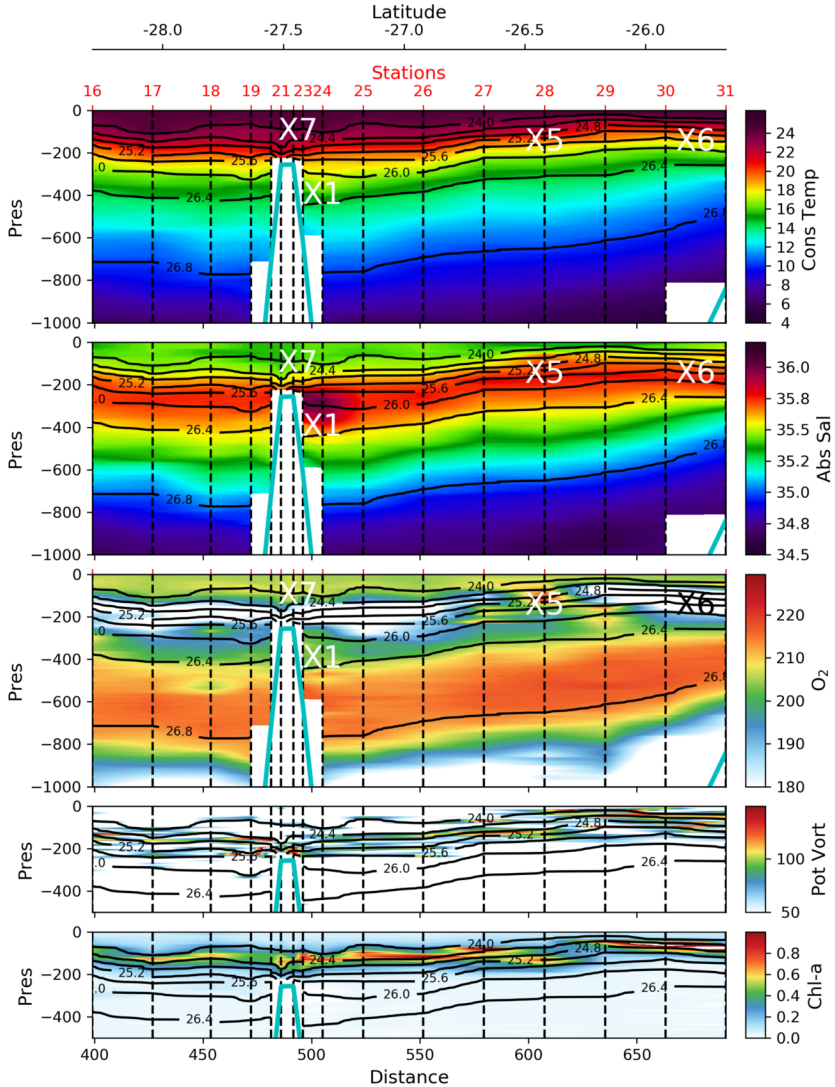
Latitude
-28.0
-27.5
-27.0
-26.5
-26.0
Stations
16
17
18
19
21
23
24
25
26
27
28
29
30
31
X7
X5
X6
X1
Pres
Cons Temp
Abs Sal
O2
Pot Vort
Chl-a
Distance
400
450
500
550
600
650

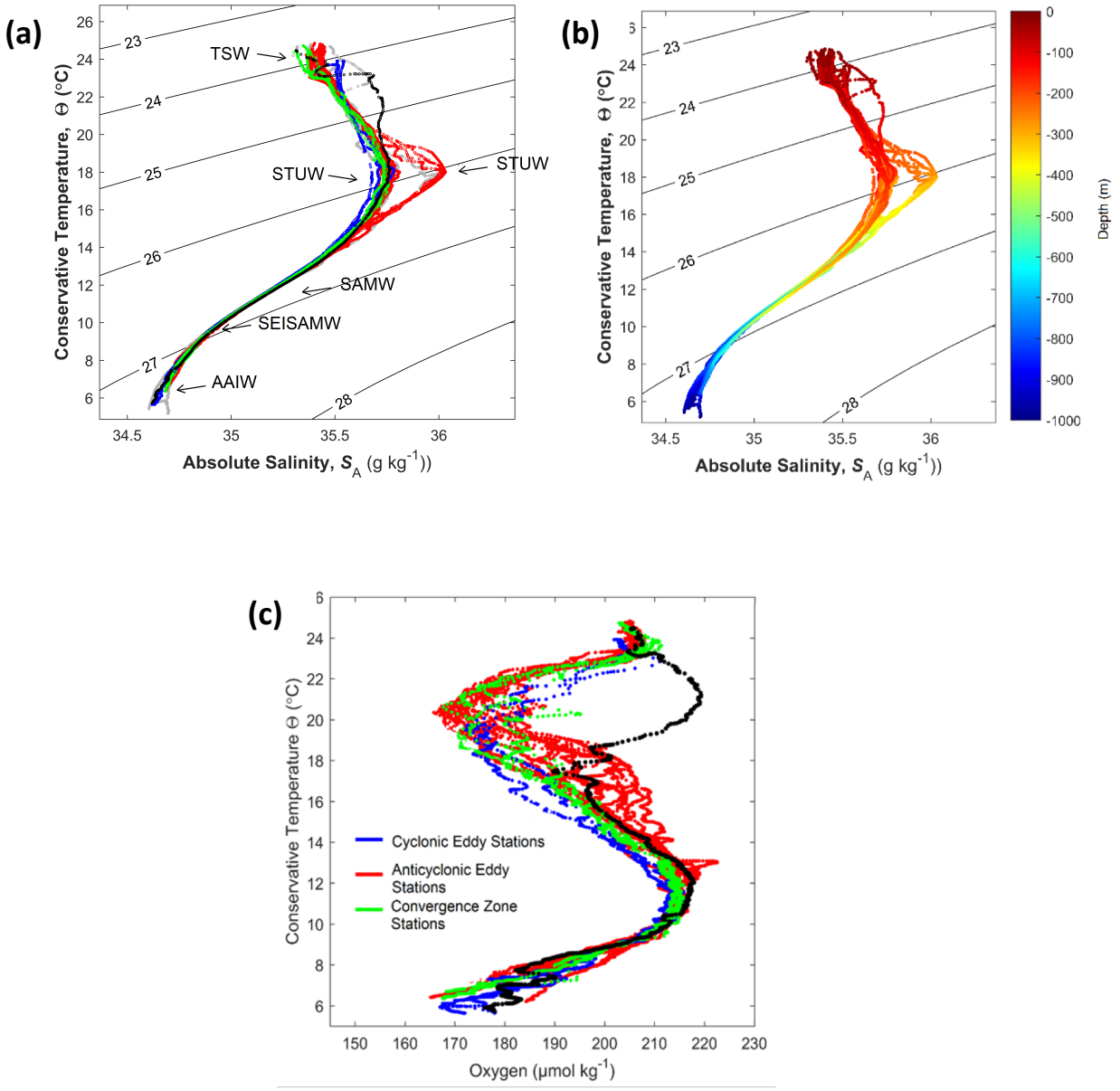
(a)
TSW
STUW
STUW
SAMW
SEISAMW
AAIW
Conservative Temperature, Θ (°C)
Absolute Salinity, S_A (g kg^{-1}))
(b)
Depth (m)
(c)
Cyclonic Eddy Stations
Anticyclonic Eddy Stations
Convergence Zone Stations
Oxygen (µmol kg^{-1})

Fig. 9

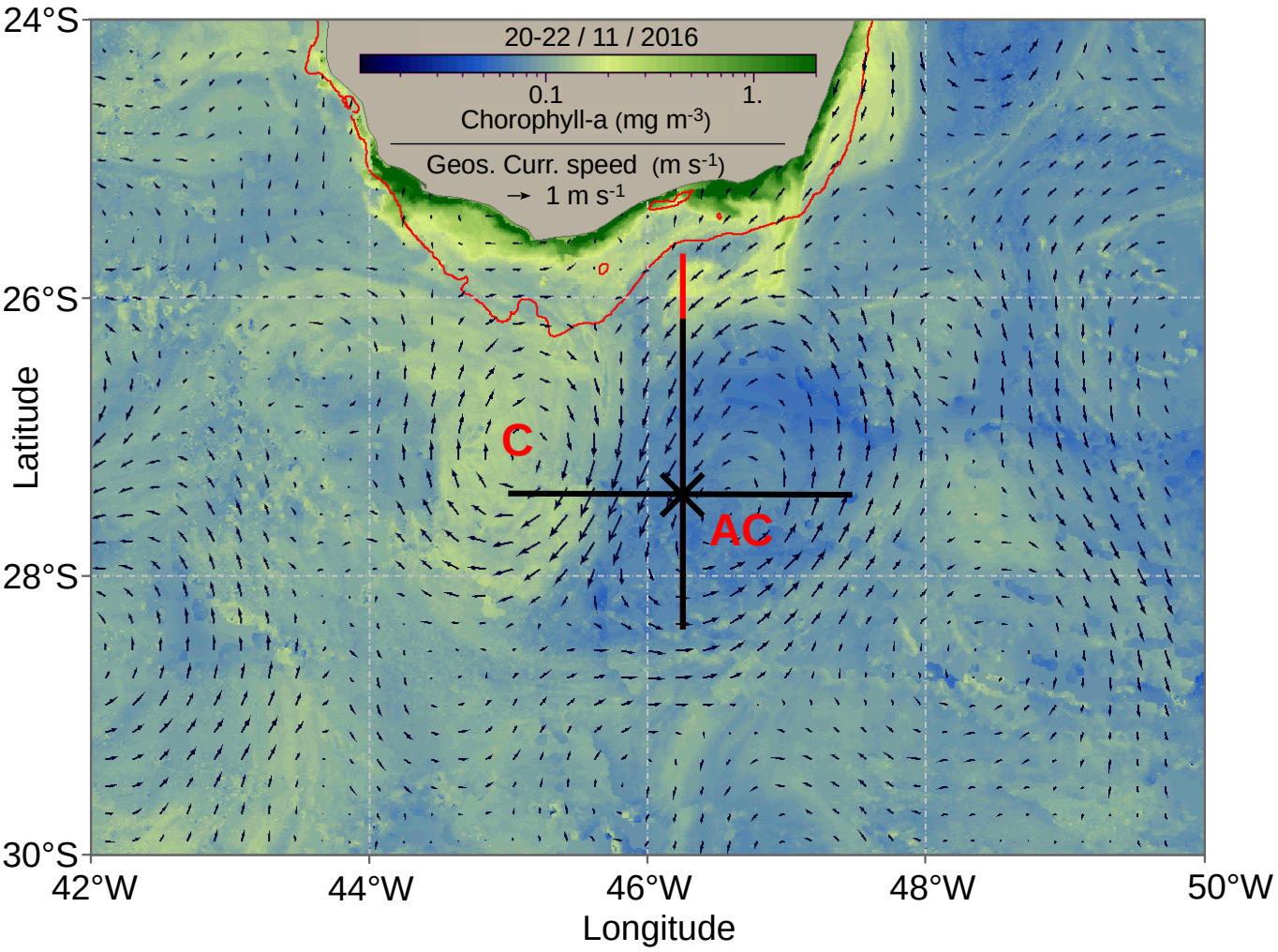
20-22 / 11 / 2016
0.1
1.
Chorophyll-a (mg m-3)
Geos. Curr. speed (m s-1)
→ 1 m s-1
C
AC
24°S
26°S
28°S
30°S
Latitude
42°W
44°W
46°W
48°W
50°W
Longitude

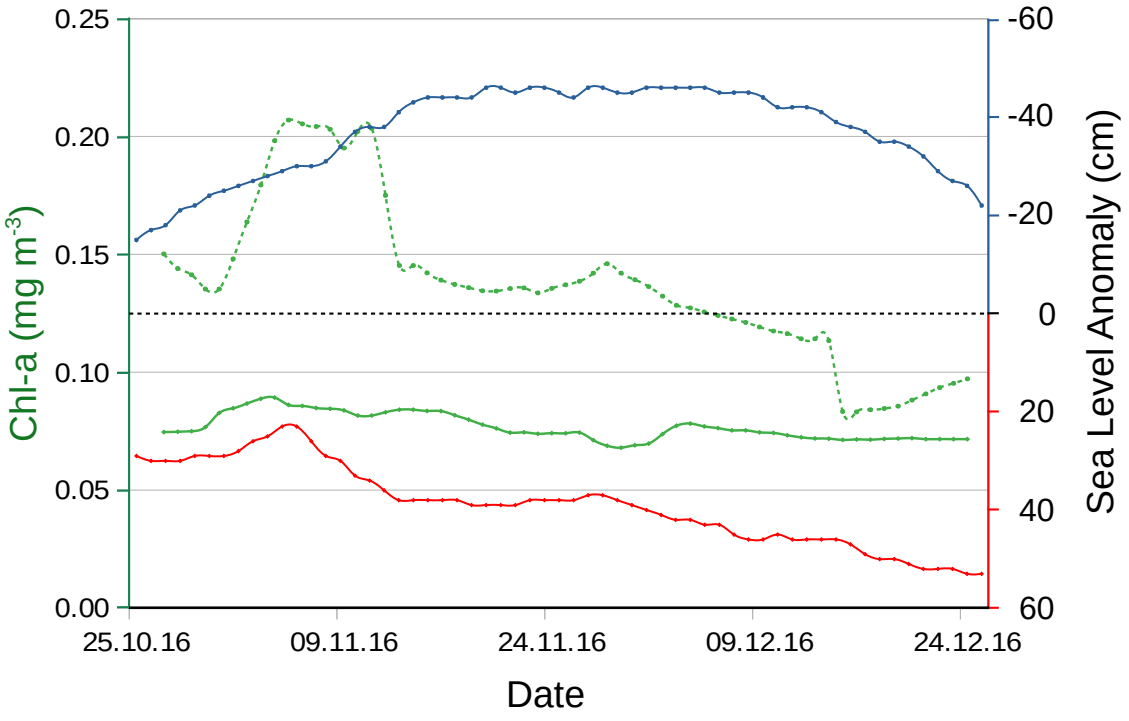
0.25
0.20
0.15
0.10
0.05
0.00
Chl-a (mg m-3)
-60
-40
-20
0
20
40
60
Sea Level Anomaly (cm)
25.10.16
09.11.16
24.11.16
09.12.16
24.12.16
Date

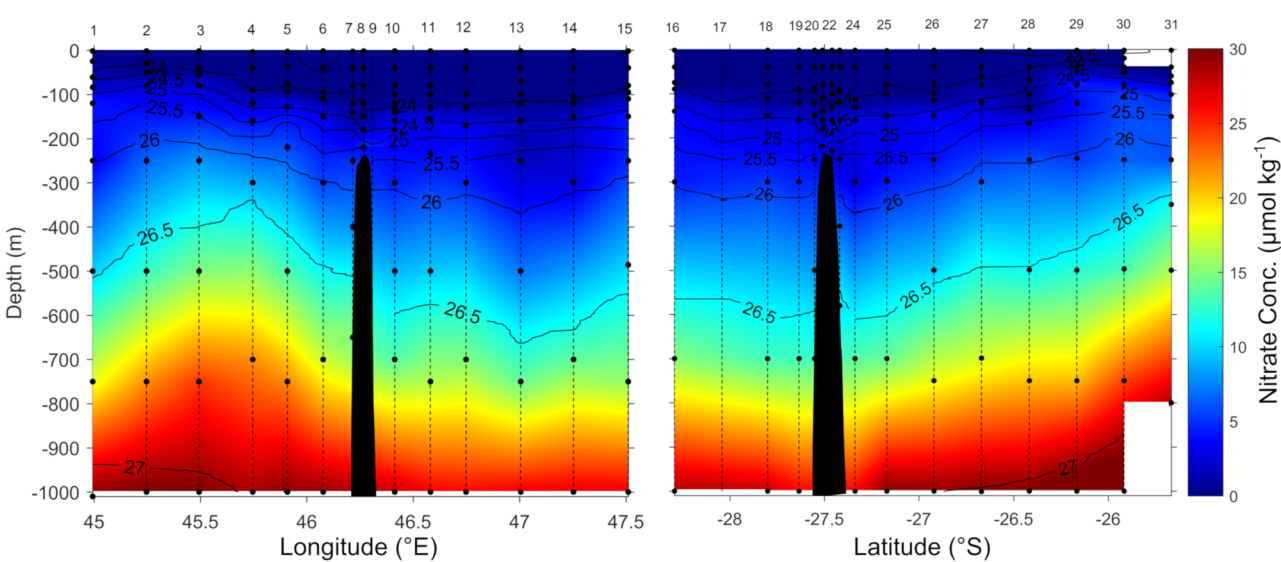
1 2 3 4 5 6 7 8 9 10 11 12 13 14 15
16 17 18 19 20 22 24 25 26 27 28 29 30 31
0 -100 -200 -300 -400 -500 -600 -700 -800 -900 -1000
Depth (m)
24 24.5 25 25.5 26 26.5 27
45 45.5 46 46.5 47 47.5
Longitude (°E)
-28 -27.5 -27 -26.5 -26
Latitude (°S)
0 5 10 15 20 25 30
Nitrate Conc. (μmol kg⁻¹)